

ADDIS ABABA UNIVERSITY
ADDIS ABABA INSTITUTE OF TECHNOLOGY
SCHOOL OF CIVIL AND ENVIROMENTAL ENGINEERING
Geodesy and Geomatics MSc Program

Monitoring of Ground Surface Deformation of Mining Area by using InSAR techniques, a case study of Midroc Lega Dembi Gold mine Shakiso, Ethiopia

By:

GEMECHU KOTOLA ADULA

ADVISOR: TULU BESHA BEDADA (Dr.)

A THESIS SUBMITTED TO SCHOOL OF GRADUATE STUDIES OF ADDIS ABABA UNIVERSITY IN PARTIAL FULFILLMENT OF THE REQUIREMENTS FOR THE DEGREE OF MASTER OF SCIENCE IN GEODESY AND GEOMATICS PROGRAM (**SPECIALIZATION IN GEODESY**).

February, 2022

Addis Ababa, Ethiopia

DECLARATION

I, the undersigned, declare that the thesis work titled "**Monitoring of Ground Surface Deformation of Mining Areas by using InSAR techniques, A case study of Midroc Lega Dembi Gold mine, Ethiopia**" is my original work completed under the supervision of **Dr. Tulu Besha Bedada,** and that it has not been submitted for a degree at any other university, and all sources of materials used for this thesis work have been properly acknowledged.

Gemechu Kotola Adula _____ _____

Name of Student Signature Date

I hereby certify that I have read and evaluated this MSc thesis

Dr. Tulu Besha Bedada _____ _____

Name of Supervisor Signature Date

APPROVAL SHEET

ADDIS ABABA INSTITUTE OF TECHNOLOGY

SCHOOL OF CIVIL AND ENVIROMENTAL ENGINEERING

The undersigned have examine the thesis entitled as **"Monitoring of Ground Surface Deformation of Mining Areas by using InSAR techniques"** presented by **Gemechu Kotola Adula**, a candidate for the **Degree of Master of science in Geodesy and Geomatics** with **specialization in Geodesy** and hereby certify that it is worthy of acceptance.

Board of Examiners Committee:

Dr. Tulu Besha Bedada	_____	_____
Advisor/Supervisor	Signature	Date
Sisay Walelign	_____	_____
Internal Examiner	Signature	Date
Dr. K. V. Suryabhagavan	_____	_____
External Examiner	Signature	Date
_____	_____	_____
Chairperson	Signature	Date

Acknowledgements

First and foremost, I want to express my gratitude to God, the creator of everything, for all of the good things that have happened to me during this thesis work and throughout my life. The Special thanks go to my supervisor and General Director of the Ethiopian Geospatial Information Institute, **Dr. Tulu Besha Bedada** for his support and guidance during the work of this study. Tulu (Dr.) was the one who encouraged me to work on this research title.

I would like to express my heartfelt gratitude to **Dr. Andinet Ashagrie** for generously sharing his knowledge for this research, for his constant guidance, support, and encouragement throughout, and for devotedly contributing to the thesis's success.

I would like to express my gratitude to the management of the Midroc Lega Dembi Gold Mine, special the Surveying and Mining section leaders, for providing ground surveying data for the validation of my research work. I would also thanks **Mr. Natnael Agegnehu** and **Mr. Andinet Nigusise** (PhD. Candidate) for their valuable encourage, comments and suggestion during SARPROZ license and data processing. **Daniele Perissin** (PhD) and the SARPROZ Admin team deserve special thanks for providing the SARPROZ license and tutorial manual.

Finally, I am grateful thanks for those people in my life who have shown courage to date and have had a tremendous good impact on my academic journey.

Abstract

Ground surface deformation caused by mining activity is a critical aspect when assessing safety of slope and environmental impacts due to the operations of open-pit and underground mining. These mining-induced ground surface deformations have the potential to seriously harm the environment, slope stability, and man-made structures in the mining activity area and this problem monitored by using either ground or space monitoring systems. Traditional or Ground methods of monitoring ground surface deformation in the mining operations region are laborious, expensive, and time consuming with in the areas that being difficult to access. Remote sensing and other geospatial observations enable a cost-effective, dependable, temporally and spatially continuous monitoring process of mining operations at enormous sizes, regardless of physical accessibility. In this study, C-band SAR data were used to demonstrate the possibility of using the Persistent Scatterer Interferometric Synthetic Aperture Radar (PS-InSAR) technique to investigate ground surface deformation induced by mining activities, specifically in the Midroc Gold Mine Company. The PSInSAR approach also has demonstrated its potential to analysis time series of ground subsidence in having dense vegetation and rural behavior of the study area. In midroc lega dembi open pit mining area, the maximum rate of ground surface deformation was −90 mm/year with a cumulative subsidence value of −200 and −100 mm were observed from InSAR techniques and −3.99866 and −0.000122 m cumulative displacement were observed from ground survey data. This large discrepancy between datasets is likely the result of dense vegetation land cover in the area of the interest. The ground survey data of the Midroc lega Dembi open pit mining region was correlated with the PS-InSAR results, revealing subsidence spots with a value of 0.98 correlation coefficient in selected point. The selected methodology of using C-band SAR data and ground survey data with PS-InSAR techniques to identify, monitor, and map ground surface deformation in the Gold mine area was practically applicable. Finally, based on the results and findings on the present study, certain recommendations has been made.

Keywords: Ground Subsidence, Open pit mining, Persistent Scatters (PS), Persistent Scatterer Interferometric Synthetic Aperture Radar (PS-InSAR)

TABLE OF CONTENTS

Table of Contents

DECLARATION..... I

Acknowledgements III

Abstract..... IV

TABLE OF CONTENTS V

List of Figures..... VIII

List of Tables X

List of Abbreviations XI

CHAPTER ONE 1

INTRODUCTION..... 1

1.1. Background of the study 1

1.2. Statement of the Problem 4

1.3. Objectives of the Study 5

1.3.1. General Objective 5

1.3.2. Specific Objectives 5

1.4. Research Questions 5

1.5. Scope of the Study..... 5

1.6. Significance of the Study 6

1.7. Limitation of the Study 6

1.8. Organization of the Thesis 6

CHAPTER TWO 8

2. LITERATURE REVIEW 8

2.1. Background 8

2.2. Ground Surface Deformation..... 9

2.3. Causes of Land Subsidence 9
2.4. Deformation Monitoring Techniques 10
2.4.1. Ground Surveying Technique 11
2.4.2. Space Geodetic Techniques 11
2.5. Application of InSAR Techniques 12
2.6. Principles of SAR and Interferometric SAR 14
2.6.1. Differential SAR interferometry (DINSAR) 16
2.6.2. Persistent Scatterers (PS) 18
2.6.3. SAR Offset Tracking 19
CHAPTER THREE 20
3. MATERIALS AND METHODS 20
3.1. Description of the study area 20
3.2. Geology 21
3.3. Data 22
3.3.1. Sentinel -1 data 22
3.3.2. Sentinel-2 Data 23
3.3.3. Ground survey data 24
3.3.4. Ancillary Data Source 26
3.4. Material and Software Used 26
3.5. Methodology and Data analysis 28
3.5.1. Processing and Stack formation 28
3.5.2. Interferometric Stacking (IS) 29
3.5.3. Processing for Resampled Displacement by InSAR techniques 30
3.5.4. PS-InSAR Processing for Cumulative Displacement 33
3.6. Normalized Difference Vegetation Index (NDVI) 37

3.7. Validation Method 38
3.7.1. Regression Analysis 38
3.8. General Methodological workflow of the Study 39
CHAPTER 4 41
4. RESULTS AND DISCUSSION 41
4.1. Resampled displacement 42
4.2. Cumulative Displacement by InSAR 44
4.3. **C**umulative displacement for the ground survey data 46
4.4. Validation 47
4.5. **DISCUSSION** 49
CHAPTER FIVE 52
5. CONCLUSION AND RECOMMENDATIONS 52
5.1. Conclusion 52
5.2. Recommendations 53
References 55
APPENDICES 64
Appendix A: Figures 64
Appendix B: Tables 70

List of Figures

Figure 3.1 Location map of the study area 20
Figure.3.2. Interferometric configurations for Ascending sentinel 1A image. 32
Figure 3.3 Interferometric Configurations for Descending Sentinel 1A images 32
Figure 3.4 ASP Graph for reference point (a) Integrated Cumulative displacement, (b) Integrated Height, (c) Integrated Residual Height and (d) Integrated Velocity. 35
Figure 3.5. Scatter plot of PS Candidate of study area for Ascending sentinel image 36
Figure 3.6. Scatter plot of PS candidate of Study area for Descending sentinel image 37
Figure 3.7. Normalized difference vegetation index map of the study area 38
Figure 3.8 Conceptual frame work of data processing. 40
Figure 4.1 Resampled Displacement of study area for Ascending sentinel-1A images 43
Figure 4.2 Resampled Displacement of study area for Descending Sentinel -1A images 43
Figure 4.3 Resampled velocity of study area for Ascending Sentinel -1A images 45
Figure 4.4 Resampled Velocity of study area for Descending Sentinel -1A images 45
Figure 4.5 Cumulative displacement map of Ascending SAR geomerty (a) and Descending SAR geometry(b) from the 2014-2016 of the study area. 46
Figure 4.6 Cumulative Displacement of Ground survey data 47
Figure 4.7 Validation of InSAR measurements and Ground survey measurements 48
Figure A.1 Data statistics for sentinel -1A ascending data sets. 64
Figure A.2 Atmosphere of reference point. 64
Figure A.3 Delaunay graph of sentinel-1A for ascending data set 65
Figure A.4 APS removal in study area of connection height, sigma connection height, connection residual height, and sigma connections residual height 65
Figure A.5 APS removal in study area of connections velocity, sigma connections velocity, and connections cumulative Displacement 65
Figure A.6 APS removal of the study area for the velocity and sigma velocity 66
Figure A.7 APS removal of the study area for the height and sigma height 66
Figure A.8 APS removal of the study area for the integrated cumulative displacement 66
Figure A.9 APS removal of the study area for the integrated residual height 67
Figure A.10 APS removal of the study area for the integrated height. 67
Figure A.11 APS removal of the study area for the integrated velocity. 68

Figure A.12 Temporal Coherence after removing the APS..... 68
Figure A.13 Temporal coherence after Graph Inversion and APS removal..... 68
Figure A.14 Selected result validation point 69
Figure A.15 Full data result validation points. 69

List of Tables

Table 3.1 Satellite information of Sentinel-1A of study area 23
Table 3.2 Ground Survey data Measurement of this study for 2014 to 2016 25
Table 3.3 Software were used in this study. 27
Table B.1 Local coordinate system ground survey data measurement of 2014 70
Table B.2 Local coordinates system Ground survey data measurement of 2016 70
Table B.3 Projected local coordinates system to UTM Coordinates system of 2014 and 2016 ... 71
Table B.4 Cumulative displacement of InSAR measurement 72
Table B.5 Ground surface displacement results for validation 74

List of Abbreviations

ALOS	Advanced Land Observation Satellite
APS	Atmospheric Phase Screen
ASI	Amplitude Stability Index
DEM	Digital Elevation Model
D-InSAR	Differential interferometric Synthetic Aperture Radar
ENVISAT	Environmental Satellite
ESA	European Space Agency
EW	Extra Wide Swath
GPS	Global positioning System
GNSS	Global Navigation Satellite System
GMES	Global Monitoring for Environmental and security Program
InSAR	Interferometric Synthetic Aperture Radar
IWS	Interferometric Wide swath
LOS	Line of sight
PS	Persistent Scatter
PSC	Persistent Scatter Candidate
PSI	Persistent Scatterer Interferometry
PS-InSAR	Persistent Scatterer Interferometric Synthetic Aperture Radar
RCS	Radar Cross Section
SAR	Synthetic Aperture Radar
SBAS	Small Baseline Subset
SLC	Single Look Complex
SRTM	Shuttle Radar Topography Mission
TOPS	Terrain Observation with Progressive Scans
VV	Vertical /Vertical
VH	Vertical/ Horizontal
UTM	Universal traverse Mercator

CHAPTER ONE

INTRODUCTION

1.1. Background of the study

Land subsidence causes ground surface deformations that have a significant impact on the surrounding environment and is one of the most prevalent yet critical challenges affecting the mining industry. Mining-related deformations can cause havoc on nearby infrastructure and buildings (Pawluszek-Filipiak and Borkowski, 2020b). Even if safe mining procedures are used the ground surface deformation is unavoidable, and it were almost certainly cause damage to nearby infrastructure. As a result, land deformation monitoring is mandated by law and is used to confirm subsidence predictions, increase extraction rates, and reduce environmental risk (Pawluszek-Filipiak and Borkowski, 2020a). Monitoring mining-induced ground deformation can also reveal small surface movements on a mine high wall, indicating signs of instability that could lead to catastrophic slope failure (Tang et al., 2020). As a consequence, effective and reliable monitoring of mining-induced ground deformation is a critical component that must be included in each active mining operation.

The main deformation monitoring systems employed by major mining operations are traditional techniques for monitoring surface movement, such as inclinometers, surveying level techniques, total station, and GNSS station and remote sensing techniques (Tang et al., 2020). The ability to make direct observations and high accuracies are two advantages of adopting traditional techniques. Unfortunately, these methods are labor-intensive, time-consuming, and expensive, and they necessitate direct access to a particular area Pawluszek-Filipiak and Borkowski, (2020b). As a result, traditional techniques are frequently limited to small, highly localized areas of a few square kilometers in high-risk situations (Yi et al., 2016). Due to the dynamic nature of a mining operation, predetermined regions may not be easily accessible, and monitoring equipment installation may be non-permanent. This can lead to significant measurement gaps and limiting a region's spatial coverage. Traditional monitoring techniques are also used in frequently and on a point-by-point basis, resulting in extremely confined spatial extent data that does not provide enough insight into the larger context of deformation patterns around a given mining operation.

Remote sensing techniques have become an important tool for assessing large-scale ground surface deformation to address these issues (Lazecký et al., 2010; Ji et al., 2016).

Differential interferometric Synthetic Aperture Radar (DInSAR) techniques enable for high-precision remote measurements of ground deformation in all weather conditions over broad areas without requiring access to a specific region (Khakim et al., 2013) . DInSAR takes advantage of phase differences between two synthetic aperture radar (SAR) acquisitions made at different times over the same area. Traditional DInSAR estimates rely on a single interferometric pair, and their accuracy is restricted by topographic and orbital errors, spatial and temporal decorrelation, and signal propagation delays caused by atmospheric aberrations and DEM mistakes/errors (Ferretti *et al.*, 2007). Furthermore, traditional DInSAR can only measure surface deformation in the line-of-sight (LoS) direction with respect to the satellite sensor. Because of the ambiguous nature of interferometric phase and temporal decorrelation, DInSAR techniques are unable to detect fast moving ground surface deformations. Previously, the D-InSAR technique employed the phase difference between radar signals acquired over time from two successive acquisitions of the study area to identify ground deformation up to the sub-centimeter scale. The primary limitations of D-InSAR techniques are: - (1) temporal and geometric decorrelation, (2) atmospheric impacts, and (3) the requirement of a precise digital elevation model (DEM). According to (Yue et al., 2011; Dong et al., 2013), temporal decorrelation is the most common cause of information loss due to dense vegetation of the mining area in the center of the ground subsidence area. To overcome these constraints, more advanced multi-temporal DInSAR approaches have been developed that incorporate more than two repeat pass SAR acquisitions.

The Persistent Scatterer (PSI) approach developed by Ferretti et al., (2001) and the Small Baseline Subset (SBAS) approach also developed by Berardino *et al.*, (2002) are two of the most popular multi-temporal DInSAR techniques. The type of targets that are identified and measured is the fundamental difference between these two techniques. As different scholar like Ferretti et al., (2001); Hooper et al., (2007); Pawluszek-Filipiak and Borkowski, (2020b) state that; the PSI approach is used to locate persistent scatterers, which are deterministic point-wise objects that contain single point scatterers with a stable phase across time. The vast majority of these objects are man-made structures or large hard surfaces. The SBAS approach, on the other hand, looks for distributed scatters, which are small groupings of pixels that belong to somewhat coherent areas in some portions of the temporal span as state by different researchers like (Ferretti *et al.*, 2011). These small clusters of pixels usually correspond to places with consistent scattering patterns, such as debris fields, non-cultivated areas, or deserts are facilitated by this approach.

The Persistent Scatterer Interferometric Synthetic Aperture Radar (PS-InSAR) technique was powerful to detect ground deformation at the millimeter level after evaluating the limitations of the D-InSAR technique. The PSInSAR technique was a geodetic Synthetic Aperture Radar (SAR) processing technique that employs two or more SAR images to generate maps of topography or deformation of the Earth's surface. This techniques applied to reduces temporal and geometric decorrelation by selecting stable points or persistent scatterers (PSs) that are temporally and geometrically coherent during the full acquisition time-series SAR data. PS-InSAR also has the ability to reduce atmospheric contribution by analyzing multi-temporal time-series SAR data with the selected PSs. Perissin and Wang, (2012) created a modified PS-InSAR (PSI) technique in which partially correlated scatterers are combined with permanent scatterers to boost the point target density in the highly vulnerable area for decorrelation. As scholars like (Guéguen *et al.*, 2009; Abdikan *et al.*, 2014; Thapa *et al.*, 2016) state that; the PS-InSAR technique has been used to detect land deformation using C-Band and L-Band SAR data in the coal-bearing area. Because of the spatial and temporal baseline of C-band SAR data is more limited than those of L-band data, the chances of temporal decorrelation are larger in C-band data (Liu *et al.* 2014). The short-wavelength C-band is better for detecting moderate velocity subsidence if the ideal baseline is maintained and the long-wavelength L-band is better for detecting rapid velocity subsidence when compare both of them. Previous research has indicated that one of the primary issues with C-Band SAR data is the low density of PSs points in the coal mine area (Kumar *et al.* 2020b).

The main purpose of this thesis is to monitoring ground surface deformation rates and cumulative displacements of the midroc lega dembi Gold mine. In this study, 52 Sentinel-1 SAR images of C-band in ascending and descending geometries and 106 points of ground survey measurements were used, as well as PS-InSAR techniques, to monitor the ground surface deformation around the Midroc lega dembi Goldfields in Shakiso, the largest open pit mine in Ethiopia. Persistent Scatterer techniques was used to measure time series ground surface deformation map around mining operations from 2014 to 2016. After that, the final cumulative displacement of InSAR data are compared to the cumulative displacement of ground survey measurement of the study area for validation.

1.2. Statement of the Problem

Minerals are extracted from under the earth's surface without extracting overburden in underground mines using the block caving, pillar process and the long-wall method. As a result, underground mining creates a vacuum underneath the Earth's crust. Roof structures are responsible for their own weight and the load of the roof structures is carried by additional supports. The roof structure-bedding plane bends when the supports are inadequate and the sag in the roof structures divides the rock structures. Fractures and spires of disturb zones form as just a result in the rock strata and the underground mining induces land deformation, which is a vertical displacement of land. Land subsidence causes cracks on the surface to form, which ultimately contribute to the creation of a cavity within the earth. As a result, during mining or after a long period the roof rock collapses and develop of the potholes on the ground surface of the mining area.

In an opencast/open pit mining scenario, however, land excavation for mineral extraction and the dumping of overburden rocks in the rim area may cause terrain instability. This is particularly true for weak and fragile rocks such as fractured shale and sandstone. Furthermore, groundwater extraction to allow opencast mining operations and the resultant decrease in the surrounding aquifer's pore water pressure triggers compaction of the aquifer and overlying rock layers. Land subsidence occurs because of this within the mining field and in open pit-mining area. This could result in the formation of large cracks in the (bench and terrace) of open pit mine and cause slope instability in mining operations area, and finally the mass wasting phenomena like landslides and debris flows. Therefore, those problems initiated by using InSAR techniques-based knowledge to identify land subsidence associated with mining activities and its consequences in the study area.

Finally, by considering the ground deformation pattern of the mining area and applying the capability of space technology, the study was monitor the ground deformation of the study area from SAR data and ground survey data; either in Long-term or short- term land deformation history can be obtained by time series InSAR data analysis.

1.3. Objectives of the Study

1.3.1. General Objective

The main objective of this study was to monitoring the ground surface deformation of mining activity area by using InSAR technology in case study of Midroc lega dembi gold mine shakiso district of Guji zone, Ethiopia.

1.3.2. Specific Objectives

- ✓ To monitor ground surface subsidence by using PS-InSAR techniques
- ✓ To evaluate the capabilities of the PS-InSAR techniques to monitor ground deformation caused by mining activity in study area.
- ✓ To validate the ground surface deformation extract from PS-InSAR with ground survey data.

1.4. Research Questions

- What is the role of PS-InSAR techniques to monitor ground surface deformation?
- How to evaluate the capability of PS-InSAR techniques in deformation monitoring.
- How to validate the result extract from PS-InSAR measurements with ground survey data?

1.5. Scope of the Study

This study aims to investigate the capability of remote sensing satellite technologies, especially the application of InSAR satellite data for deformation monitoring, in light of current ground surface deformation monitoring practices. The study was assess deformation with a sub-millimeter level of precision using InSAR techniques.

The scope of this research is to assess the feasibility of using InSAR-based systems for ground surface deformation monitoring in general, as well as the usefulness of such systems in identifying various types and degrees of ground surface subsidence of midroc lega dembi gold mine. However, in the literature review section, all recent efforts on InSAR-based ground subsidence monitoring are briefly described.

1.6. Significance of the Study

InSAR technology is used in this study to map ground surface deformation across the midroc lega dembi gold mine. This thesis work's scientific achievements can be classified into three groups. The first is the contribution to ground deformation science in which the observe, describe, and simulate a variety of ground deformation phenomena in order to learn about different geophysical processes, some of which have never been observed or realized before, with a focus on ground deformation induced by man-made factors and its activity. The second is the contribution to ongoing scientific research in this study area in both as a location and as a topic. The third is a contribution to the technique for using InSAR observations in man-made deformation studies, which would be of interest to researchers who use InSAR data to investigate a variety of geophysical and man-made issues. The other significant aspect of subsidence is that it is a complex topic with multiple strategies, technological aspects, and governance implications. As a result, it needs early warning system which is critical for alerting local authorities, industry, and government agencies before significant ground surface, construction, and infrastructure subsidence happens. In order to manage ground surface subsidence the concern body should be develop appropriate strategies and measures that are both effective and efficient in the short and long term, and an integrated approach is required.

1.7. Limitation of the Study

The present study made every attempt to obtain the necessary information through primary and secondary data collection, analysis, and interpretation. However, there are certain limitations of this study; one of the most difficult limitations of this investigation was the shortage of resources and the limitation of data in this study area during the downloading of Sentinel-1A (S-1A) data from the Copernicus/Alaska facility website. Another challenge to become trained was the newness of the PS InSAR analysis methodology. Nevertheless, this study gives vital information and insight that can be quite useful for ground surface monitoring in mining area.

1.8. Organization of the Thesis

This thesis is deals with the integration of space technology datasets and ground survey measurement for monitoring ground surface deformation in mining area and organized in five chapters: the first chapter introduces about basic concept of ground surface deformation due to mining activities and their effect to the environment, society and infrastructure; describe the

statement of the problem, state the objectives of the study, scope of the study and as well as the limitation of the study. Chapter two is an extensive review of literature pertaining to the need for ground surface deformation monitoring, the causative factors of ground surface deformation with monitoring ground deformation techniques, includes a few major applications of SAR Interferometer to monitor different natural disasters and measure displacement, as well as past results using the similar techniques and methods for different periods. Chapter three; It presents the research design and methodology. It is a description of the study area; it is focusing on data acquisition Processing and presentation, the details about the amount, type and basic information about the satellite data that were used. Additionally, it describes the general idea of SAR Interferometry and how it is applied as well as the methodology on which the processing was based on. Chapter four; it presents interferometric SAR processing results with their ground truth and mining activity interpretation, and points out only one test site areas in the study area. The results produced by the processing of the data in the form of maps and time series graphs. Also, it includes the comparison of InSAR results with ground survey measurements. Chapter five presents extracted conclusions and recommendation made to develop the key points and the outcomes of the research.

CHAPTER TWO

2. LITERATURE REVIEW

The importance of mapping surface deformation for better understanding subsurface structural behavior and subsidence trends is discussed in this chapter. Following that a description of surface deformation monitoring methods is presented, with a focus on approaches that use microwave SAR remote sensing data and observations.

2.1. Background

The configuration of the Earth's surface reflects practically all of the processes that occur at or near to the surface, as well as those that occur deep in the crust, and that regulate the exterior shape of that changes due to subsidence and rising to some extent. Surface deformation is determined by the geology of the area, as well as the properties of the soil and its thickness. The depth and thickness of the layer that experienced depression, as well as the properties of the above strata, determine the extent of ground deformation Nassir, (2019). Several geodetic techniques, such as leveling and InSAR, can be used to determine surface deformation. InSAR is the most effective approach for monitoring ground deformation with the needed spatial and temporal completeness; it produces a consistent deformation map of the Earth's surface with sub-centimeter accuracy (Wang *et al.* 2019). It's also a cost-effective method. For more than two decades, optical and microwave satellite images have been collected to observe, evaluate, and estimate natural resources around the world. Microwave satellites, unlike optical satellites, do not acquire images using sunlight. Furthermore, because to lower levels of atmospheric attenuation, they utilize a specific region of the electromagnetic spectrum that can penetrate heavy clouds, fog, and dust in any weather condition. Synthetic Aperture Radar (SAR) is a microwave remote sensing method that has been used to quantify the surface reaction to ground deformation in various locations. SAR in general and interferometric SAR in particular, have been used to measure regional-scale land subsidence. One objective of employing surface deformation data is to manage or prevent risk related with land surface deformation. High-resolution mapping of spatiotemporal deformation fields can reveal key details regarding source geometries and physical processes Anderssohn *et al.*, (2009). Following that, there is a discussion of several Surface deformation monitoring techniques. These include SAR remote sensing capabilities from orbit as well as InSAR processing techniques.

2.2. Ground Surface Deformation

Land subsidence is mostly caused by active underground mining and subsurface coal fires. Furthermore, due to the presence of voids and weak supporting pillars of earth surface, ground subsidence can occur at any time on existing mine workings, regardless of how long they have been neglected was studied by (Sahu and Lokhande, 2015). Surface deformation can be caused by natural or manmade sources, and it can occur over a wide variety of time periods, from near-instantaneous settlement (seismic, volcanic, and glacier movement) to progressive mild displacement resource extraction. Mining, groundwater, oil and gas extraction can all cause it. It can also be localized or large-scale. These can result in a variety of major environmental risks, including infrastructure collapse, bridge damage, and changes in river and groundwater flow paths. These risks not only endanger people's lives and property, but they also have a significant influence on the national economy. Local surface deformation may have the most immediate impact on critical surface infrastructure and its long-term development Zhang *et al.*, 2019; He *et al.*, 2020). Regional ground settlement, on the other hand, contributes to an increased risk of coastal flooding, seawater intrusion, changes in groundwater systems, and the reactivation of regional faults (Nagel, 2001; Alfarrah and Walraevens, 2018). As a result, measuring and monitoring ground surface deformation is critical for both current and future development planning.

Surface deformation, its size, direction, and causes are evaluated and predicted using a variety of techniques (Galloway and Burbey, 2011). Ground-based or remotely sensed geodetic surveys, such as tilt meters, GPS, leveling, InSAR, and LIDAR, are commonly used to map relative changes in the elevation or inclination of the ground surface.

2.3. Causes of Land Subsidence

The main causes of land surface subsidence are active groundwater extraction, underground mining, and open pit mining and subsurface coal fire. Furthermore, one of the causes of land subsidence is the weight of buildings and infrastructure, but it can happen at any time over active volcanic areas and natural gas extraction (Robertson et al., 2012). Surface subsidence occurs because of many forms of subsurface mining and particular methods that deliberately cause the mined void to collapse, such as pillar extraction, long wall mining, and any metalliferous mining process.

The most severe damage to the natural environment, structures, and infrastructure is caused by surface compressive and tensile strains, curvature, tilts, and horizontal displacement. The other reason is natural gas extraction. As natural gas is extracted from a natural gas field, the field's initial pressure (up to 60 MPa (600 bar) decreases over time. Ground subsidence may be occurs because of the fluid withdrawal when:- 1) reservoir fluid pressures are reduced, 2) reservoir rocks are compactable and/or unable to effectively resist deformation when load is moved from the fluid phase to the grain-to-grain contacts, and (3) the overburden lacks internal self-support, the formations can easily deform downward (Robertson et al., 2012). There was even an earthquake. During an earthquake, land subsidence can occur in a variety of ways. Because of the balance along fault lines, large areas of land was subside dramatically during an earthquake. Land subsidence may also occur as a result of unconsolidated soil settling and compacting as a result of earthquake shaking. The Japan Geospatial Information Authority confirmed immediate subsidence occurred in Japan and observe different result of the in different study area in Tohoku earthquake in 2011. Ground Subsidence of 0.50 m (1.64 ft.) was observed on the Pacific Ocean coast in Miyako, Tohoku, in Japan. While 0.29 m (0.95 ft.) was observed in the south in Soma, Fukushima of Japan. On other hand the Oshika Peninsula in Miyagi Prefecture, the highest amount of ground subsidence 1.2 m (3.93 ft.) was observed with horizontal diastrophism of up to 5.3 m (17.3 ft.). In many coastal towns, such as Jakarta, Bangkok, and Shanghai, ground water exploitation is one of the leading causes of land subsidence (Aimaiti et al., 2018).

The subsidence (or sinking) of land caused by groundwater extraction is known as groundwater-related subsidence. Lowland habitation, such as coastal or delta plains, necessitates drainage. The subsequent aeration of the soil causes the oxidation of its organic elements, such as peat, which can contribute to substantial land subsidence. Clay is found in large amounts in many soils. If the amount of seasonal drying exceeds the level achieved by building foundations, they was move, potentially causing damage to the structure in the form of tapering cracks.

2.4. Deformation Monitoring Techniques

Nowadays, monitoring and analyzing ground surface deformation is an important branch of geodesy science. There are two major types of techniques: geodetic and non-geodetic techniques. This classification is based on whether you're calculating absolute or relative displacement. The aim of geodetic techniques is to calculate the absolute displacement of a point or area relative to a

stable reference point, while the goal of non-geodetic methods is to assess the relative deformation of a point or area relative to neighboring points or areas (Javad et al., 2019).

2.4.1. Ground Surveying Technique

Geodetic techniques, which are based on measuring dereferenced displacements in one, two, or three dimensions, provide global information on the behavior of the system. It usually provides enough redundancy of observations for statistical quality assessment and error detection. Total stations, levels, Interferometric Synthetic Aperture Radar (InSAR), and global navigation satellite system receivers are among the instruments and techniques used (Kalkan, 2002). Non-geodetic methods, on the other hand, provide localized and geographically disrupted information without any verification unless they are compared to other measurements.

Non-geodetic instruments are also well suited to automated and continuous tracking. Extensometers, piezometers, pressure meters, rain gauges, thermometers, barometers, tiltmeters, accelerometers, and seismometers are among the instruments Kalkan, (2002). Until the early 1980s, traditional measuring methods were the only way to detect deformation. This satellite-based positioning technique was used to detect deformation after this time by establishing GPS measurements in geodetic and surveying applications.

This was a pivotal moment in the field's use of remote sensing data (Erol and Erol, 2002). Although the GPS technique has high accuracy in three dimensions, it has a flaw in vertical positioning due to inherent geometric and atmospheric errors (Featherstone, 1998; Celik, Rennie and Akinci, 2011). As a consequence, using GPS measurement to track deformation with sub-centimeter precision necessitates the use of various methods, such as the rapid static method or the creation of special equipment for short baselines or accurate antenna height readings.

2.4.2. Space Geodetic Techniques

There are different space geodesy techniques like LLR, SLR, VLBI and InSAR to determine the ground surface deformation. In my case, this study was used InSAR techniques to investigate the ground surface deformation in mining industry. Imaging from space Synthetic Aperture Radar (SAR) systems are microwave-based active sensors that can track the surface in any weather condition without the need for solar illumination. They can simultaneously calculate amplitude and phase, with phase values relating to sensor-target distance. Atmospheric artefacts and

geometric effects distort SAR images over topographically rugged terrains; the latter can be enhanced by looking at the same position from different acquisition geometries. The fundamental concepts of SAR as an imaging method and interferometric SAR as a technology for extracting ground surface deformation rate from SAR images are presented in the following section.

2.5. Application of InSAR Techniques

The range of applications for InSAR is extremely broad, and it is rapidly expanding over time:

-In seismology, land surface deformation induced by earthquakes; Funning et al. (2005) studied SAR Interferograms formed by Envisat ASAR data to construct a three-dimensional displacement field of the deformation caused by the 2003 earthquake in Bam (Iran). The majority of the fault motion detected by InSAR happened on two faults, a concealed strike-slip fault running beneath the center of Bam and a second, obliquely slipping fault whose surface trace is close to the previously mapped Bam Fault, according to the results of their modeling. Furthermore, the scientists claim that the geometry of these two faults, which are anticipated to meet and interact at deep, is comparable to that of other earthquakes in eastern Iran.

According to Calais *et al.* (2010) used a mix of geodetic (GPS) and remote-sensing (InSAR) techniques to investigate the 7.0 Mw earthquake in Haiti's Port-au-Prince region in 2010. As this researcher state that; the Ground motion data revealed that the earthquake involved both horizontal and contractional slide, resulting in transpressional motion. Moreover, the earthquake created an unexpected contractional deformation, and the pattern of strain accumulation indicated that faults other than the known ones in the area were active. Instead, the earthquake was caused by an unmapped north-dipping fault known as the Léogâne fault, according to the authors. According to interferometry observations of ground Subsidence the earthquake involved a combination of horizontal and contractional slide to creating transpressional motion. This finding is in line with Hispaniola's long-term pattern of strain accumulation.

-In natural disaster monitoring and assessment: Volcanoes and landslide movement; one of the first applications of interferometric techniques to monitor volcanic activity yielded reliable results (Massonnet et al., 1995). A study of Mt. Etna in Italy, which was conducted from 2000 to 2005, is an example of the method employed in volcanology (Solaro et al., 2010). The study covered the years 1994 to 2008 and includes data from a variety of sensors, such as the ERS-1/2 and Envisat. The results of the SAR data processing were divided into different periods of activity and

fault mechanisms. They also revealed widespread flank instability, which was by far the most common type of deformation at Mt. Etna, regardless of the volcano's status (magma storage, dike emplacement, inactivity).

In terms of other natural disasters, (Liu et al., 2012) used InSAR time series to study significant landslide dangers in China's Three Gorges region. The study included three independent groups of Envisat ASAR images (a total of 85), each of which was processed separately. The resulting maps showed that the InSAR time-series technique was successful in identifying surface deformation in the study region by displaying consistent linear movement trends, allowing the identification of two discrete landslides with varied moving patterns and magnitudes.

-In mining: land subsidence as a result of mining; According to Paradella et al. (2015) evaluated a stack of 33 TerraSAR-X images to provide a synoptic and informative perspective of the deformation processes affecting the Carajás complex (Brazil) as a result of mining activities. The majority of the mining complex was stable during the TerraSAR-X coverage period, however substantial deformation rates were found over waste dumps and several pit slopes, according to deformation maps. Furthermore, the authors stated that using space-based SAR in conjunction with field monitoring devices was important for operational mining planning and risk assessment. (Bountzouklis, 2016) demonstrated that the ability of Differential Synthetic Aperture interferometry (DInSAR) to locate the damaged areas caused by mining subsidence in a vegetated region of New South Wales in Australia by utilizing a series of ERS-1, ERS-2, and JERS-1 radar images for interferometric processing. ERS-1 (longer wavelength) data for mine subsidence monitoring are more robust in the presence of vegetative or agricultural ground cover than ERS-1/ERS-2 (shorter wavelength) data, and also more suitable for the area undergoing high rate ground deformation. Shorter wavelength data, on the other hand, is far more sensitive to mine subsidence. Finally, the authors stressed that the methodology provides a cost-effective, dependable, and operational supplement to existing ground survey methods when properly adjusted for atmospheric conditions.

-In environmental and structural engineering: ground subsidence and structural stability was studied by (Parcharidis et al., 2015) to evaluated the stability of the multi span cable-stayed bridge between Rio and Antirio, Greece, as well as the surrounding area. They were able to extract qualitative information on the temporal displacement pattern of the Rio-Antirio Bridge as well as

quantitative measures of deformation accumulation rates using Envisat ASAR and TerraSAR-X StripMap satellite data. The implications of the findings are fruitful since, as demonstrated, the methodology used can be extended to other risky situations, such as dams.

Di Martire et al. (2014) described how DInSAR algorithms were used to track the ground deformation of the Conza Dam in the southern Apennines (Italy). In this study the researchers use 51 Envisat ASAR images and found a high level of agreement between the final DInSAR displacements and in-situ instrumental data, demonstrating the technique's reliability for precise monitoring of civil infrastructures, particularly dams with a high exposure factor and associated risk.

-In forestry: Forest canopy height, mapping, and monitoring are all important aspects of forest management. Between June 2011 and August 2012, study carried by (Askne et al., 2013) was evaluate the spatial distribution forest and estimation accuracy of biomass across the hemi-boreal test site of Remningstorp in Sweden using eighteen interferometric Synthetic Aperture Radar (SAR) image pairs acquired from the TanDEM-X mission. In the case of forest conditions like those in Remningstorp, the presented analysis demonstrated that TanDEM-X InSAR data combined with an accurate high-resolution Digital Terrain Model (DTM) has been the potential to estimate and map the surface-ground dry biomass with high accuracy.

-In ground water hydrology: land subsidence caused to excessive water pumping or uplift due to ground water recharge; a research was done by (Raucoules et al., 2002) in 2002 to monitor the urban subsidence in the city of Prato (Italy) caused by excessive water pumping for industrial reasons in the study region. During the years 1993-2000, the study team employed six ERS-1 and ERS-2 images to create four interferograms. Based on the interferometric combinations, the subsidence phenomenon in the area appeared to be continuous across the seven-year period, with a maximum value of about 8.3 cm. The researchers believe that InSAR could be useful in land use planning and natural risk assessment.

2.6. Principles of SAR and Interferometric SAR

SAR is a type of imaging radar that detects the return of a target's actively emitted microwave signal. This imaging technology does not rely on solar irradiation due to the existence of microwave energy as an illuminating source in radar sensors, making it more flexible than conventional passive optical and spectral sensor technologies. In terms of illumination of the

ground surface, radar signals are unaffected by darkness or clouds, and hence can acquire information largely irrespective of surface and atmospheric conditions. SAR may generate an electromagnetic field with a fixed phase relationship between the values of the electric field at various locations and times. It can also record amplitude and phase information for a ground target at the same time Nassir, (2019). The amplitude and phase information of ground scattering elements illuminated by the radar pulse are expressed by a matrix of complex numbers in the on-board integration of backscattered signals.

The phase information is dependent on the distance between the phase centers of the radar antenna and the terrestrial target, while the amplitude data is dependent on the sum of returned energy from each resolution cell or image pixel. Different polarizations (i.e. temporal variation or oscillation) of the electric field associated with each radar pulse in a specific plane can be recorded in SAR data. Polarization can be done in linear-single or dual-polarization modes, as well as more advanced full-polarimetric modes. While a single polarization SAR transmits and absorbs polarized radiation vertically (VV) or horizontally (HH), a dual polarization SAR produces two linear polarization combinations (HH, HV) or two polarization combinations (HH, HV) (VH, VV). Full-polarization systems that have recently become available are designed to transmit two orthogonal polarizations and record all received polarizations (HH, HV, VH, and VV) (Cloude, 2009). In comparison to traditional single or dual polarization, full polarization SAR systems may provide a complete scattering matrix, allowing significant information to be extracted from the image and separating surface scattering from dihedral scattering in more vegetated areas (Shirvany, 2012). The acquisition geometry is related to the coordinates of each pixel in a SAR image in terms of range and azimuth directions. The azimuth direction is orthogonal to the moving platform path, while the range direction is orthogonal to the path. Off-nadir or look-angle (θ) is the inclination of the radar antenna with respect to the nadir, which is never zero but varies from around 20 to 50 degrees. SAR systems' ability to alter the off-nadir angle is critical for adapting to mountainous terrain, which is a possible obstacle to InSAR. SAR acquisitions are collected in the slant-range direction, which is the direction in which the sensor's Line of Sight (LOS) travels.

In other words, the true vertical movement and the east-west portion of horizontal movement can be calculated using data obtained by satellites in both ascending and descending orbits. Since the process of SAR image acquisitions over the same area at different times varies, this can be used to

retrieve ground motion over vast remote areas where ground-based observations are difficult to come across Bu et al., (2000). InSAR, as one of the most common uses of SAR imagery, is focused on superimposing two images to produce a new image that displays topography and changes in ground levels with millimeter-level precision, as well as random orbital error, temperature, and background noise interferences (Massonnet and Feigl, 1998; Duro et al., 2013). Interferometric SAR (InSAR) displacement data are the result of integrating several SAR scenes acquired at a height of 514 km. The surface displacement between the phases can be calculated by comparing the phase signal from repeat-pass SAR acquisitions and applying various filtering techniques (Gabriel et al., 1989).

The calculations are accurate to a fraction of the sensor's wavelength. An interferogram is the difference in phase between two SAR scenes. Surface deformation (ΔφDispla), difference in atmospheric path delay (ΔφAPS), topography (ΔφTopo), and other noise contributions (Δφdecorr) all contribute to the phase difference (Δφ) in an interferogram, which is measured in radians from 0 to2π:

$$\Delta\varphi = \Delta\varphi topo + \Delta\varphi displa + \Delta\varphi atmosphere + \Delta\varphi noise \quad (1)$$

To find the surface deformation component (ΔφDispl) of the total phase difference in an interferogram (Δφ), topographic contributions (ΔφTopo) are removed using a Digital Elevation Model (DEM), and atmospheric contributions (Δφ APS) are removed using filtering techniques such as the small baseline (SB) method (Berardino et al., 2002), and persistent scatterer interferometry (PSI) method. During the interferogram's time span, the phase portion is converted to mm displacement. The distance between the two orbits (perpendicular baseline,B ⊥) determines the topography part (Δφtopo). To reduce sensitivity to topography, interferograms with small perpendicular baselines are preferred. Other noise effects (Δφdecorr) are caused by changes in the geometrical or dielectric properties of the surface cover (temporal decorrelation) and phase contributions caused by baseline differences (spatial baseline decorrelation) (Henderson et al., 2011).

2.6.1. Differential SAR interferometry (DINSAR)

DInSAR techniques was used for the two or more Synthetic Aperture Radar (SAR) images were acquired at different times with the same or a corresponding sensor from approximately the same

aspect angle in repeat-pass DInSAR. The resulting images have nearly identical speckle in certain regions, and the phase difference is due to the difference in imaging path length. The phase difference is calculated by using the normalized Interferograms argument, when $\boldsymbol{\gamma}(\boldsymbol{normalized\ Interferograms})$ which is defined as the normalized complex correlation coefficient of the complex backscatter intensities of SAR images. The magnitude of the normalized Interferograms $\gamma = |\boldsymbol{\gamma}|$ is used to determine the degree of coherence, which is a measure of phase noise. Surface topography and coherent displacement along the look vector that occurs between the acquisition of the interferometric data pair affect the interferometric process. The main sources of error are inhomogeneous propagation delay and phase noise.

The basic concept behind the DINSAR method is to isolate the effects of surface topography and coherent displacement, allowing displacement maps to be retrieved. This is done by eliminating the topography-related phase, which is either simulated or calculated from an independent interferograms based on a Digital Elevation Model that is accessible (DEM). A DEM is typically more reliable and operational, so it is used more frequently. Interferometric phases are only known modulo 2π from complex valued interferograms. As a consequence, phase unwrapping is a critical step in estimating unambiguous differential interferometric phases. The interferometric process is extremely sensitive to surface deformation. 2π displacement phase corresponds to just 2.8 cm displacement along the look vector in the case of a C-band SAR (ERS, ENVISAT, and Radarsat). It is referred to (Bamler and Hartl, 1998; Rosen, 2000; Wegmüller et al., 2000) for a more detailed introduction to DINSAR. The atmospheric path delay term limits the accuracy of the ground deformation estimated from the single differential interferograms.

The atmospheric path delay was one of the most atmosphere artifacts that affects the accuracy of the deformation estimated from single differential interferograms. Interferogram stacking is a well-known technique for reducing this error. Interferogram stacking was the basic principle is to combine several results into a single result. The key assumption is that the deformation process is strongly correlated, whereas the error terms (atmosphere, signal noise, and baseline related) are uncorrelated between independent pairs. This isn't entirely accurate (for example, the topography-related atmospheric error term), but it's a common assumption. While the independent terms' signal terms add linearly, the error terms add at a slower rate since they are uncorrelated, resulting in a lower error in the stacked result. As shown in, it is possible to achieve mm/year accuracies for

relatively slow uniform deformations in urban areas by combining ample observation time (Strozzi et al., 2000; Tosi et al., 2002). One of the most significant pre-requisites is the availability of suitable pairs with appropriate time intervals and short baselines. It's also worth remembering that the spatial coverage is limited to the spatial coverage of individual results (Huang et al., 2015; Borghero, 2017).

2.6.2. Persistent Scatterers (PS)

The PS technique is particularly useful and appropriate for urban analysis, as it produces angular structures and efficient reflectors that dominate background scattering. In 1999, Ferretti developed the Persistent Scatterer Interferometry (PSI) technique for the analysis of urban structures and building deformation. By interpreting time-series of interferometric phases at coherent point dispersed, the PSI method allows us to quantify deformation with uncertainties of one millimeter per year (Ferretti et al., 2000, 2001). Using a large number of stacked images, the PS approach generates different interferograms with regard to a single common master image. The PSI method works by defining pixels whose scattering properties are relatively constant over time and angle of view. Pixels dominated by a single scattered fit these requirements best; hence, images are processed at maximum resolution to increase the likelihood of only one dominant scattered being present, as well as to minimize the contribution of other scattered within each pixel Sousa et al., (2008).

PSs' electromagnetic stability allows for DEMs with a 1-m accuracy Perissin et al., (2011) and millimetric terrain motion estimates (Ferretti et al., 2011). By evaluating alternative interferometric combinations, the Quasi-PS (QPS) technique was recently introduced to extract information from scattered and decorrelating targets. The physical nature of the targets has been investigated because a clear understanding of the PS physical nature is a crucial step in correctly interpreting the measured deformation process (Perissin and Rocca, 2006) . By combining all of the steps with time series of InSAR images, each coherent pixel can be linked to a specific target. PSs are stable artificial targets that are typically found in mining industry environments, so their lifespan and density can be used to characterize mining activity in terms of space and time. The advantages of time series of InSAR images can be obtained in two ways with a daily revisiting cycle: 1) Since PS is linked to artificial targets, different PS birth times that reflect urban growth

can be calculated using ground displacement, and 2) each PS can be linked to the physical characteristics of a single goal.

Since the scattering characteristics of these pixels differ significantly with look angle, the PS approach is less optimal in images where most pixels contain several scattered of similar intensity. While PS-InSAR deformation measurements are extremely accurate, this does not always mean that the parameters of interest are accurately calculated. PS-InSAR deformation measuring approaches may measure a variety of deformations, including gas extraction, shallow compaction, and structural instabilities, however unambiguous interpretation is difficult.

2.6.3. SAR Offset Tracking

In contrast to InSAR, offset monitoring estimates surface velocity both along the satellite's flight path and along the satellite's LOS-direction. The offset tracking technique, which is widely used to observe glaciers, estimates displacement by comparing and tracking patterns (speckle-tracking) based on the amplitude part of the obtained complex backscattered signal (Strozzi et al., 2002; Rignot et al., 2011; Sund et al., 2014). With offset monitoring, the smallest detectable deformation is between 1/10 and 1/20 of the resolution.

CHAPTER THREE

3. MATERIALS AND METHODS

3.1. Description of the study area

The southern part of Ethiopia, especially the Adola and Magado belt, has been a target for gold and base metal exploration for many years. Midroc lega Dembi and Sakaro are found in this part of the country and the most one of the explored Gold mines currently under operations. In 1997, the MIDROC Technology Group's subsidiary firms, paid 172 million dollars for the government to privatize the Midroc Lega dembi Gold mine. The research area is located in the Oromia Regional State, Guji zone, oddo shakiso locality about 500 kilometers south of the capital city Addis Ababa. The midroc Lega Dembi gold mine is bounded by 5° 42' 00"−5° 44' 00"N latitudes and 38° 52' 30"−38° 54' 30"E longitudes covering a total area of 144 km^2 (Figure 3.1). Midroc lega dembi open pit mine is the leading gold deposits from the country and the climate is moderately seasonal with significant diurnal temperature fluctuations.

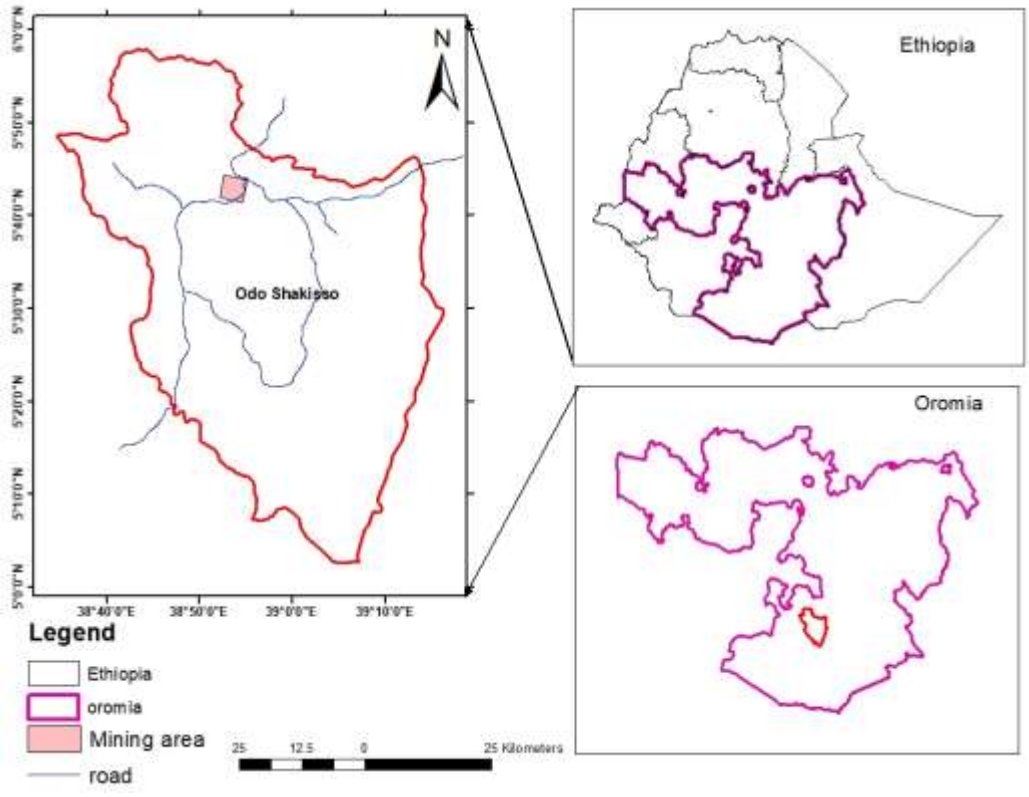


Figure 3.1 Location map of the study area

3.2. Geology

Significant shear belts in southern Ethiopia include the Adola Belt's north-south trending fold systems, orogen parallel north-south trending, and oblique NW-SE regional strike slip shear zones (Getaneh, 1994; Billay et al., 1997). The volcanics and sediments that make up the Adola greenstone belts developed as a result of extreme tectonic activity. In the Adola region, geological structures such as foliations, folds, faults, joints, and shear zones are common (Tadesse, 1999; Adamu, 2018). On the eastern limb of the Lega-dembi graben-syncline, the study area is located. In the granite-greenstone terrain of Adola, at least three major deformation events occurred. The Lega dembi gold deposit is situated along the contact between quartzo-feldspathic gneisses and metasediments in the Lega dembi-Aflata shear zone. In the Lega dembi region, there are three sets of faults: one that runs north-south, another that runs north-east, and a third that runs north-west. However, apart from these fault systems, the region is known for small-scale E-W faults Tadesse, (1999). The main ore zone is divided into parts by normal faults trending NW, NE, and E-W (South, central, north and upper Lega dembi). Lega dembi Valley is dominated by the area's linear north-south trending structures (faults). Sakaro's structural development is comparable to Lega dembi's Tadesse, (1999); Wube, (2005). The Wollena valley is bounded on the northwest by faults Ghebreab et al., (1993). Lega Dembi deposits are mostly found on or near the eastern edge of the Megado volcano-sedimentary belt. Within the Megado belt and surrounding gneissic terrane, five major deformations have been identified: D1 - an early gneissosity-forming occurrence in the gneissic terrane, expressed as early folds in the Megado belt, associated with a compressive thrust; D2 - which resulted in regional north south trending upright folds, which are the region's dominant structural grain and are linked to an east-west contractional occurrence. D3 - as a result of a NW-SE directed transpressional event to strike-slip shearing along the greenstone-gneissic domain contacts D3 was occurred. In case of D4 – as a result of east-west trending, uplift, moderate to steep easterly and/or westerly plunging folds was occurred, as discussed by some authors to be the result of D3 transpressional shearing; D5 - late, brittle NW-SE and NE-SW to east-west trending faults that interrupt the granite-greenstone terrane's north-south pattern. As a result, during the analysis of ground surface deformation in this study area, they cannot consider the geological deformation pattern of the study area because the deformation analyzed was the man-made deformation.

3.3. Data

Various types of data were applied in this study to assist us in effectively and efficiently completing the analysis of this research. The most prevalent type of data were used is InSAR data and Ground Survey data. SENTENIEL radar data have been released by ESA as part of a data collection package. In both SAR level zero and SLC data set formats, this data set is available on the ESA virtual archive website. These details was used to assess the study's objectives.

3.3.1. Sentinel -1 data

After 2012, the Global Monitoring for Environment and Security program, formerly known as GMES was renamed as a Copernicus. The European Commission (EC) is leading a project to construct a new family of satellites dubbed Sentinels in collaboration with the European Space Agency (ESA). These satellites was deliver a unique set of observations starting from Sentinel 1 SAR data in all-weather both day and night.

Interferometric Wide Swath (IWS), Extra Wide Swath (EW), Wave (WV), and Strip map (SM) are the four modes in which Sentinel-1's radar equipment can operate. Different polarization schemes can be used with those modes. The polarization of the Wave is single mode (VV or HH), Dual polarization (VV + VH, or HH + HV) as well as single polarization are available for all other modes (VV or HH). The default mode over land is the interferometric broad swath mode, which has a swath width of 250 kilometers and a ground resolution of 5 x 20 meters. The Terrain Observation with Progressive Scans SAR images in three sub-swaths in this mode (TOPSAR).

Two stacks of Sentinel-1 images were gathered for 2014 and 2016 to examine the capabilities of InSAR time series algorithms and to estimate land deformation. There are 27 ascending geometry images for 2014-2016 and 25 ascending geometry images for 2014-2016. Because of its susceptibility to rough surface scattering, VV polarization was selected to improve land surface detection. With pixel spacing of 2.3 meters by 14.1 meters and a swath width of 250 kilometers, all images were taken in Level-1 Single Look Complex (SLC) IW mode. All images in a collection must be acquired along the same track to be compatible with InSAR processing.

Images are not discriminated against in this stage because of their perpendicular or temporal baselines. The sensor's short repeat period (12 days) makes it easier to track deformation around mining zones with low temporal decorrelation. Despite this, the mining operation's non-coherent

nature causes even this little temporal variation to result in a loss of coherence that is too great to reliably quantify deformation within the mine using repeat-pass images. Furthermore, due to scattering of the short wavelength (5.6 cm) within dense vegetation surrounding the location, there is still a significant loss of coherence.

To achieve the overall objectives of the study, as illustrated in below Table 3.1 two datasets of Single Look Complex (SLC) Sentinel-1A ascending and descending scenes, each with 27 and 25 images which cover the period from October 2014 to December 2016 were employed .

Table 3.1 Satellite information of Sentinel-1A of study area

No	Parameters	Description	No	Parameters	Description
1	Image type	Sentinel -1A	1	Image type	Sentinel -1A
2	Acquisition pass	Ascending	2	Acquisition pass	Descending
3	Image in number	27	3	Image in number	25
4	Product type	SLC	4	Product type	SLC
5	Acquisition mode	IW	5	Acquisition mode	IW
6	Polarization	VV	6	Polarization	VV
7	Sub-swath	2	7	Sub-swath	2
8	Wavelength	5.6cm	8	Wavelength	5.6cm
9	Acquisition time	October 2014 – December 2016	9	Acquisition time	October 2014 – September 2016

3.3.2. Sentinel-2 Data

The European Space Agency (ESA, 2015) launched the Sentinel-2 optical imaging mission as part of the Copernicus program. The Sentinel-2A and Sentinel-2B are two polar orbiting satellites that launched by European space agency to achieve the Sentinel-2 mission. The optical imaging sensor Multi-Spectral Instrument is installed on each satellite (MSI). Sentinel-2 satellites offer images between 443 and 2190 nm in the visible and infrared spectrum, making them ideal for land surface observation (Gascon, 2012). Sentinel-2A was launched in 2015, followed by Sentinel-2B in 2017

(Shimizu et al., 2020). The scanning width of 290 km and a resolution of up to 10 m are appropriate for detecting changes in vegetation and making harvest forecasts, mapping forest stands, and estimating the growth of wild and cultivated plants, according to (Team, 2015). In this study, level -2A products of sentinel-2 were used for normalized difference vegetation index (NDVI) to estimation for the effects of vegetation on ground surface deformation monitoring in the study area.

3.3.3. Ground survey data

Total stations are surveying equipment that can precisely and accurately measure the locational position of artifacts, architecture, and terrain in archaeological sites and regions and the ground survey data of this study is collected through total station and EDM. Because of its high precision and provision of the three-dimensional components of the deformation field, the total station is one of the most suited approaches for measuring ground surface deformations (East-North-Up). However, due to a lack of collected ground survey station density (point stations per unit area) and corporate working security, the collected ground survey data from the firm's survey department, which is a significant restriction of this method. As a result of the continuous coverage of interferograms, combining InSAR and total station data to map very accurate deformations (i.e. at sub-centimeter levels) with unparalleled geographical coverage is a very effective approach. Thus, data covering the study period from 2014 to 2016 stations placed on the open-pit region were obtained from survey section to assist the research aims, available for two separate years as illustrated in below Table 3.2. In this study 106 points of ground survey data were observed for both years i.e. 2014 (68 points) and 2016 (38 points), but 38 points of ground survey data was used to easily monitor ground surface deformation with the same years and the same numbers of points. For this investigation, the time series data were obtained using a local coordinate system and projected to WGS1984 or UTM.

Table 3.2 Ground Survey data Measurement of this study for 2014 to 2016

Year of observation		2014		2016		
No.	Northing	Easting	Height	Northing	Easting	Height
1	5996.766	5361.732	1959.562	5700.843	5522.133	1937.918
2	5971.65	5371.223	1959.476	5700.082	5508.91	1939.525
3	5980.467	5398.782	1960.157	5698.275	5493.493	1938.416
4	5924.717	5417.333	1959.629	5698.378	5477.764	1938.61
5	5919.697	5409.416	1958.775	5695.782	5455.726	1939.119
6	5911.893	5393.393	1959.074	5694.912	5430.816	1941.408
7	5910.376	5391.2	1959.831	5739.063	5520.402	1940.305
8	5851.577	5410.504	1960.227	5739.829	5485.052	1939.178
9	6050.644	5394.754	1959.068	5749.797	5432.579	1941.447
10	5915.064	5485.951	1958.787	6013.735	5408.177	1949.514
11	5595.609	5502.118	1950.453	6001.958	5365.04	1950.546
12	5614.95	5537.681	1949.306	5964.754	5377.19	1949.769
13	5374.616	5847.754	2028.57	6090.594	5353.719	1950.01
14	5381.704	5789.232	2021.108	6090.253	5332.538	1951.329
15	5487.734	5715.29	2009.448	5725.841	5582.815	1979.973
16	5546.813	5629.947	1998.645	5547.06	5529.62	1960.389
17	5572.725	5606.713	1994.035	5686.668	5416.379	1961.071
18	5677.815	5611.884	1984.11	5866.936	5401.131	1960.049
19	5681.421	5613.09	1983.765	6090.587	5325.123	1961.248
20	5739.663	5606.926	1979.243	6092.438	5324.435	1962.221
21	5836.272	5563.344	1968.287	5940.595	5485.755	1980.61
22	6094.816	5368.624	1960.29	5725.841	5582.815	1979.973
23	6099.028	5316.767	1970.538	5364.698	5604.13	1920.013
24	6053.663	5322.394	1969.318	5284.613	5633.315	1920.805
25	5988.176	5346.605	1971.016	5287.339	5654.005	1929.078
26	5756.56	5409.428	1961.992	5344.245	5640.446	1919.244
27	5517.856	5519.341	1961.143	5370.971	5660.629	1919.208
28	5196.059	5997.48	2047.466	5427.7	5612.404	1920.245
29	5208.123	6001.855	2046.181	5435.189	5601.711	1919.815
30	5234.006	5992.24	2045.428	5438.655	5598.214	1920.09
31	5326.146	5859.669	2032.481	5439.951	5597.064	1920.772
32	5347.394	5855.411	2030.399	5444.371	5594.183	1921.413
33	5349.826	5854.745	2029.122	5448.764	5590.12	1921.394
34	5356.834	5773.547	2024.321	5451.917	5586.049	1921.589
35	5489.127	5684.467	2008.838	5455.5	5583.805	1922.026
36	5572.828	5581.784	1992.704	5454.993	5581.301	1921.536
37	5704.261	5593.632	1983.488	5451.531	5578.511	1921.694
38	5996.766	5361.732	1959.562	5700.843	5522.133	1937.918

3.3.4. Ancillary Data Source

3.3.4.1.DEM

Using a precise DEM of the study area, the topographic phase signature is eliminated from interferograms (Hooper *et al.*, 2004). Three pass interferometry (Massonnet and Feigl, 1998) can be used to build such a DEM, or it can be collected from other sources or technologies such as photogrammetry. Before June 29, 2009, the most complete and homogeneous available DEM with the highest resolution for the entire world was created by the Shuttle Radar Topography Mission (SRTM) (Farr *et al.*, 2008). For the United States and its territories, SRTM DEM is available in one arc second (about 30 m spatial resolution) and three arc seconds (approximately 90 m and also one kilometer spatial resolution) internationally. In this study, one arc second DEM which is automatically downloading from the SARPROZ software package was used.

3.3.4.2.Orbital parameter

Relevant agencies or universities provide orbital parameters of SAR satellites for repeat pass interferometry, also known as orbit files, in preliminary precision processing and accuracy levels. To remove the orbital phase signature from interferograms, researchers employed precise orbit information created by the European Space Agency (ESA) using the Doppler Orbitography and Radio Positioning Integrated by Satellite (DORIS) approach. According to Sandwell et al., (2008), exact orbits are given with the leader file of L1.0 products, as 28 state vectors with better than one meter accuracy, and they are available three days following data acquisition. In this study the orbital parameters are downloading from SARPROZ software package automatically during the export all content of sentinel -1A SLC product in to preliminary steps.

3.4. Material and Software Used

In the previous section, they looked at the characteristics and requirements of interferometric processing techniques and satellite observations, and this study were employed different software as illustrated in below Table 3.3 for two identical satellite data acquisitions in both C-band microwaves. SARPROZ software packages are used for the PS analysis. Sentinel-1 data is imported, preprocessed, and exported using SARPROZ because it is delivered in its original file format and must be exported to *.KML and GeoTFF before being processed using another software like MATLAB and ArcGIS.

The interferogram and PS map are then geocoded by the SARPROZ program and displayed on Google Earth. To find the correlation coefficient and RMSE, the validation analyses were carried out by using Microsoft office, Mathcad and another software. Finally, ArcGIS or MATLAB tools were used to combine the data and create a more accurate ground subsidence map.

Table 3.3 Software were used in this study.

No	software	Version	Accessibility	Purpose
1	SARPROZ	Pcodes	Purchased (Licensed for one Years)	✓ Used to implements in a wide range of SAR, InSAR and multi-Temporal processing techniques. ✓ It's also used for SAR/InSAR data investigations and analysis. ✓ Used for monitoring the natural and man-made deformation activity
2	ArcGIS	10.7.1	free	❖ In this study; ArcGIS used for: ✓ To generate surface elevation and extract point values of ground survey data with respect to InSAR measurement. ✓ To map location of the study area ✓ To prepare or map cumulative displacement of ground survey data result.
3	Matlab	2017a	free	✓ Used for project local coordinate system into global coordinate system ✓ To map the cumulative displacement of the study area.
4	Microsoft office	2016	free	✓ Used for organizing and write the document of the study. ✓ Used for statistical calculation.

3.5. Methodology and Data analysis

In this study PS-InSAR techniques was applied. The principles of PS-InSAR technique were explained in the latter part of the section. The PS-InSAR processing was carried out by using SARPROZ software. SARPROZ can process long time series data using a variety of methods (Perissin and Wang, 2012; Ruiz-Armenteros *et al.*, 2016). The method can detect deformation in locations where the number of coherent targets (i.e. PSs) during the entire study time period is very low due to decorrelation in the study area. The processing chain on which the whole PS-InSAR processing was based on is presented in detail and illustrated below Figure 3.8. These measurements were later validated by processing Ground survey data of 2014 and 2016 of series measurement and comparing these to the InSAR results.

3.5.1. Processing and Stack formation

Importing the raw Sentinel-1A data is the first step in the processing. Downloading of the orbit data, which includes the satellite's instant location and velocity, is an extra step that is not always required (depending on the SAR satellite) and automatically downloading a Digital Elevation Model (DEM) is the next step in the process. It is worth noting that the DEM is an integral component of the processing chain since it is used in both the critical step of co-registration and the step of interferogram generation. Interferometry with Sentinel 1 SLC data requires a high quality and accurate co-registration of the SLC pairs, so the processing strategy for co-registration of a pair of S1 TOPS SLC is important (Prats-Iraola *et al.*, 2015). The method used in SARPROZ software, the selected image (master) that was used as a basis to co-register the rest of images is slave image in the ascending and descending datasets respectively. The pixel offsets between the master and slave images that occurred during the co-registration process for the ascending and descending datasets. The generation of coherence for each interferometric pair is another interesting result of this step. Using the imported DEM, the topography phase parameter was also omitted from the differential interferograms. To improve the efficiency of the phase unwrapping step, an adaptive phase filtering method (Goldstein et al., 1988) was applied to all differential interferograms. The process of restoring the right multiple of 2π to each point of the interferometric phase image is referred to as phase unwrapping. The unwrapped phase can be evaluated by a straightforward path-independent integration of the phase differences of nearby wrapped phases starting from a reference position and assuming that all phase differences are in the interval ($-\pi$,

π). However, due to phase steps outside of the interval (-π, π), phase unwrapping is more difficult in real interferograms. i) Phase Noise (temporal decorrelation, shadow, and poor SNR), ii) Phase Discontinuities (layover and discontinuous surface deformation), and iii) Phase Under-sampling generate local phase gradients greater than π (Werner et al., 2003).

After completing phase unwrapping, a baseline refinement step is required to achieve better accuracy on the values of perpendicular baseline between all interferometric pairs. This step recalculates the initial baselines using the wrapped and unwrapped differential interferograms that have already been formed. The interferograms are re-formed after the refining procedure, but this time with updated baseline values for each pair.

To complete the processing chain, the interferograms are reformed following the refinement process; the step was transformed to displacement using knowledge of the topography from the DEM. Finally, the displacement along the SAR look vector corresponds to the differential interferometric phase are calculated.

3.5.2. Interferometric Stacking (IS)

Stacking differential interferograms is focused on measuring the average phase of two or more interferograms over a given time scale to minimize decorrelation factors that trigger phase variability and extract common details. Interferometric stacking was the most basic procedure to calculate linear combinations of different interferograms which are formed as single interferograms (generally sums or averages the single interferograms). The stacking technique is extremely helpful in overcoming the shortcomings of traditional InSAR, which are caused by two negative decorrelation factors: low coherency over long temporal separations and atmospheric influences (Bountzouklis, 2016).

Low coherency over long temporal separations: When adequate coherency levels over long time periods are impossible to achieve, many short time-period temporally-contiguous interferograms can be summed to produce a pseudo-interferogram over a longer time period. This allows for the long-term monitoring of low-rate displacements in the absence of a single coherent interferogram.

Atmospheric influences: When many differential interferograms covering an instantaneous event (such as an earthquake or other abrupt ground displacement) exist, they can be summed to increase

the signal (displacement) to noise ratio (atmospheric). As a result, the stacked interferogram produced largely comprises phase associated with deformation phenomena and less phase associated with decorrelation components. However, excluding the affected interferograms from the approach is sometimes the only reliable way of removing atmospheric effects (Bountzouklis, 2016).

A reference point on the scene must be defined when using this form. The reference point is a point with zero phase that is used to calculate the relative change rate of differential phase for the entire image. The point's position is decided on the basis of two criteria: a) putting the point on areas with high coherence values, and b) putting the point on areas where the relative deformation is very low. As the contribution of phase errors due to atmospheric and baseline error increases, the inaccuracy of the phase rate was usually grow with increasing distance from the reference point. The reference point is used to estimate all differential phases.

When calculating the phase rate, the individual interferogram phases are weighted by the time interval. The basic principle is that atmospheric data remain constant from one observation to the next. As a result, the standard deviation of a single interferogram's phase rate is proportional to 1/delta T. (time interval). The average linear differential phase change rate is depicted by the IS principle (phase rate).

3.5.3. Processing for Resampled Displacement by InSAR techniques

The main principle of InSAR interferometry is to compare the phase of two or more radar images obtained at different times from the same flight track. This is used to calculate the wavelength scale of resampled displacements of the Earth's surface. In a non-vertical LOS direction, SAR satellites observe the ground. The phase information can only be linked to the LOS displacement in a zero-baseline state, while in fact, a baseline is always present, rendering the interferogram sensitive to topography.

With the use of an external DEM the topographic phase contribution was eliminated from the interferogram, by producing a Differential SAR interferogram that can be utilized to detect small changes in the range distance between two acquisitions (e.g. deformation). The determination of phase difference is needed for SAR interferometry phase component and phase unwrapping INSAR analysis and deformation detection, so accurately obtaining phase difference and

evaluating the component affection the overall phase change is important. As shown below, five components contribute to the phase difference of the SAR image:

$$\Delta\varphi = \Delta\varphi Displacement + \Delta\varphi elevation + \Delta\varphi flat + \Delta\varphi atmosphere + \Delta\varphi noise \quad (2)$$

$\Delta\varphi Displacement$: Contribution of surface deformation to the interferometric phase and the change was measured.

$\Delta\varphi Elevation$: Contribution of topographic effects to the interferometric phase in the elevation form is eliminated

$\Delta\varphi flat$: Effect of earth curvature to the phase this effect can be estimated and subtracted

$\Delta\varphi Atmosphere$: Due to temperature, humidity, and atmospheric changes in pressure between acquisitions, the atmosphere contributes to the interferometric phase.

$\Delta\varphi noise$: The phase noise due to temporal change of the scatters and look angle.

After subtracting the phase contributions from elevation, Earth curvature, noise, and atmospheric influence, the signal remaining is primarily the range change due to surface deformation, which can be written as range change Nassir, (2019).

$$\varphi def = \left(\frac{4\pi\Delta R}{\lambda}\right) \quad (3)$$

In this work only Interferometric Stacking Module were done where the SLC file are extracted and provides an orbital parameter in order to select input files for master and slave image to create coherence image for processing single interferogram image. Interferogram calculation were done by Using the SARPROZ software package and generated 53 coherent interferograms in sentinel-1A including phase unwrapping and topographic phase removal based on the SRTM-1 digital elevation model (DEM) using equation 2 and equation 3. In order to improve fringe visibility resulted from reduction of noises, adaptive radar interferogram filter of Goldstein filtering technique were applied. When the conversion between radar coordinate system to geographic coordinate system occurred, the unwrapped interferometric phases was transformed (geodetic projection on WGS 84 datum). This stage produces a collection of unwrapped filtered interferograms that reveal phase variations caused by changes in ground motion level. So here in below Figure.3.2 and Figure *3.3* shows the generation of interferogram starting from one single

master image connected with each individual image to create a best coherence according to their spatial and temporal base line.

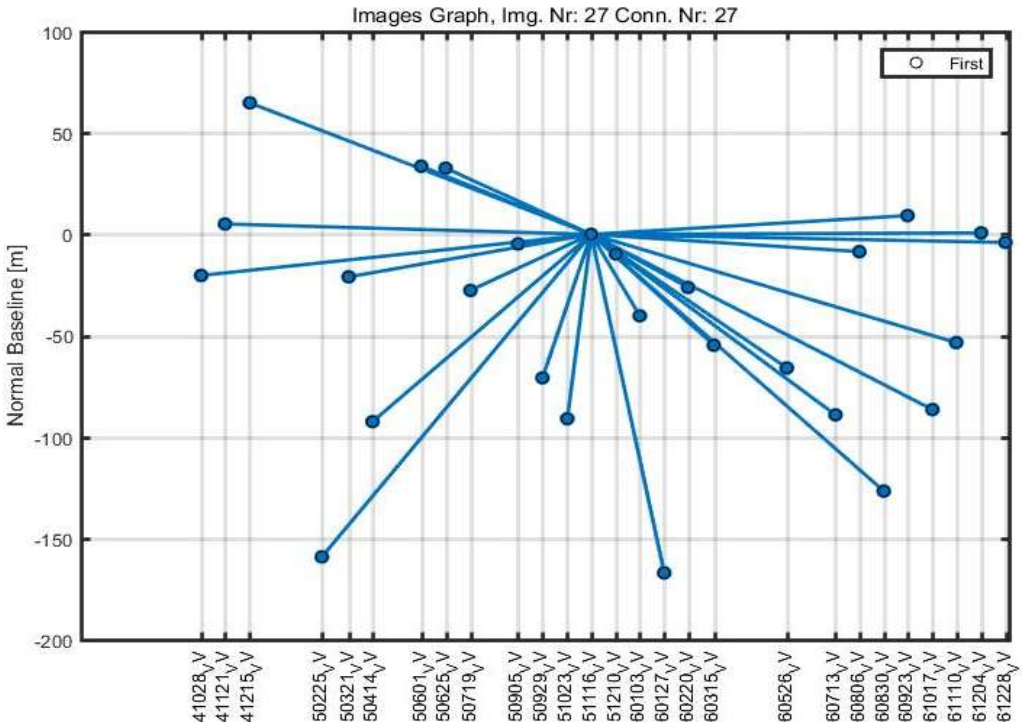


Figure.3.2. Interferometric configurations for Ascending sentinel 1A image.

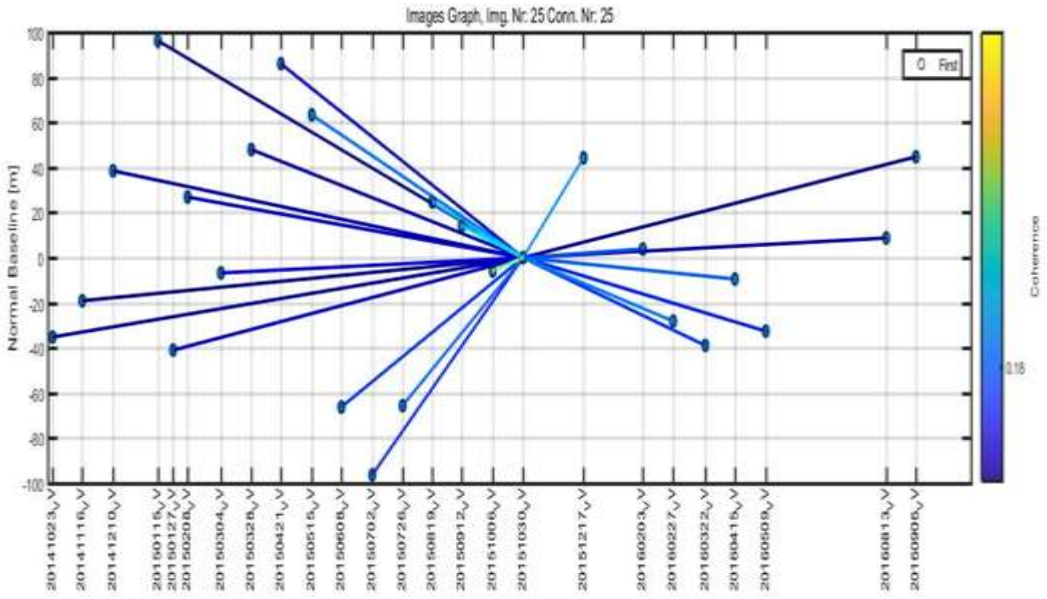


Figure 3.3 Interferometric Configurations for Descending Sentinel 1A images

3.5.4. PS-InSAR Processing for Cumulative Displacement

Persistent Scatter (PS-InSAR) approaches make use of interferograms with a single master and only use coherent pixels of stable phase or amplitude (Ferretti et al., 2001; Hooper *et al.*, 2004). PSI is used to measure the displacement without compromising precision and resolution, in order to resolve decorrelation and atmospheric in homogeneities (Crosetto *et al.*, 2016).

The method provides the spatiotemporal evolution of a process of instability. These pixels are called Persistent Scatters (PS) when the response to the radar is characterized by a strong signal coming from a principal reflecting object and it is constant over time; when the response is constant over time but the signal comes from various small objects, the pixels are called Distributed Scatters. For detecting displacement changes over time, the PSI approach uses a spatial subset of the data with the most accurate phase information. The process creates an interferogram image from a large number of scenes obtained over the same region with the same acquisition parameters. After all interferograms have been calibrated to the reference point of the study area, the stacking of the image and time series analysis have been performed. To begin, interferogram displacements at each pixel are used to generate deformation rate-maps for each dataset, which are then scaled to give annual vertical displacement rates. The method uses a large number of scenes acquired over the same area greater than 20 pair of to make an interferogram image with the same acquisition parameters. After all interferograms are adjusted to the reference point of the region the next step was, then perform stacking and time series analysis was done. In this steps, first the interferogram displacements are generated at each pixel to create deformation rate-maps for each dataset and that are scaled to give cumulative rates of vertical displacement.

After these preliminary operations, the two datasets were processed once again independently using an opposite module that is specific for PSI analysis of small areas. The scene was then cut to keep only the open-pit and the surroundings, for a total area of ca 1 km^2. The starting point of the multi temporal analysis is the reflectivity map, which represents the average intensity (i.e. amplitude) and it is the result of the average of all the dataset. The reflectivity is displayed in a grayscale map, where bright areas are indicators of stable reflection of the radar signals.

For each pixel is calculated the Amplitude Stability Index, which is based on the concept of the amplitude dispersion DA, but normalized from 0 to 1.

It is defined as:

$$Amp.Stab.Index = 1 - \frac{\sigma}{\mu} = 1 - DA \quad (4)$$

In simple words, the higher is the standard deviation (i.e. less stable is the point in time), the lower is the value of the stability index, and vice versa. There is no compulsory value that must be used as threshold, as it depends on the circumstances, but typically points are considered reliable with ASI around 0.7−0.75 and higher (Ferretti et al., 2001).

The study area is highly vegetated, so the points which were selected as Permanent Scatterers (PSs) had an Amplitude Stability Index which was lower compare to other studies which use the same method and software but in different regions with in less vegetation (e.g. Roque et al., 2015).

In this study, the PS candidates were identified creating a mask using both the Amplitude Stability Index threshold and temporal coherence set to 0.6 and 0.6 and a Reflectivity threshold 2 and 2 for both two the descending data and the ascending data sets respectively. These values were adopted in order to obtain enough points in the area especially on the open pit mining despite the vegetation. If the ASI threshold would have been higher, no points would have been available for the analysis. On the other side, the Reflectivity threshold is different for each dataset simply because in correspondence with the open pit mining area, the reflectivity range is different in the ascending mode compare to the descending mode. In the ascending mode 1481 candidates were found, while in the descending mode it increased to 1496 points respectively.

PSI relies on a subset of dependable pixels known as Persistent Scatters (PS) because not all data points (pixels) show consistent phase changes. The selection criteria for data include high scattering value pixels that are consistent across all scenes. Even for interferometric pairings with very long geometrical baselines, the phase values of these scatters are estimated in all interferograms, which are generated from all scenes with regard to a master image (larger than critical baseline). The density of the scatters distribution plays a significant effect in the quality of the displacement analysis.

PSI has been found to be effective in urban areas with strong structure reflectors and a high scatters dispersion density. However, because the PS targets density is low, the approach is less successful in open spaces. PS candidates (PSC) were selected for full-site investigations based on a mixture of quality parameters relevant to radar signal stability, such as reflectivity, the Amplitude Stability

Index (ASI, i.e. the amplitude coefficient of variation), and spatial coherence. To retrieve and remove the Atmospheric Phase Screen, a network of PSC was developed to estimate the preliminary height and velocity parameters (APS).

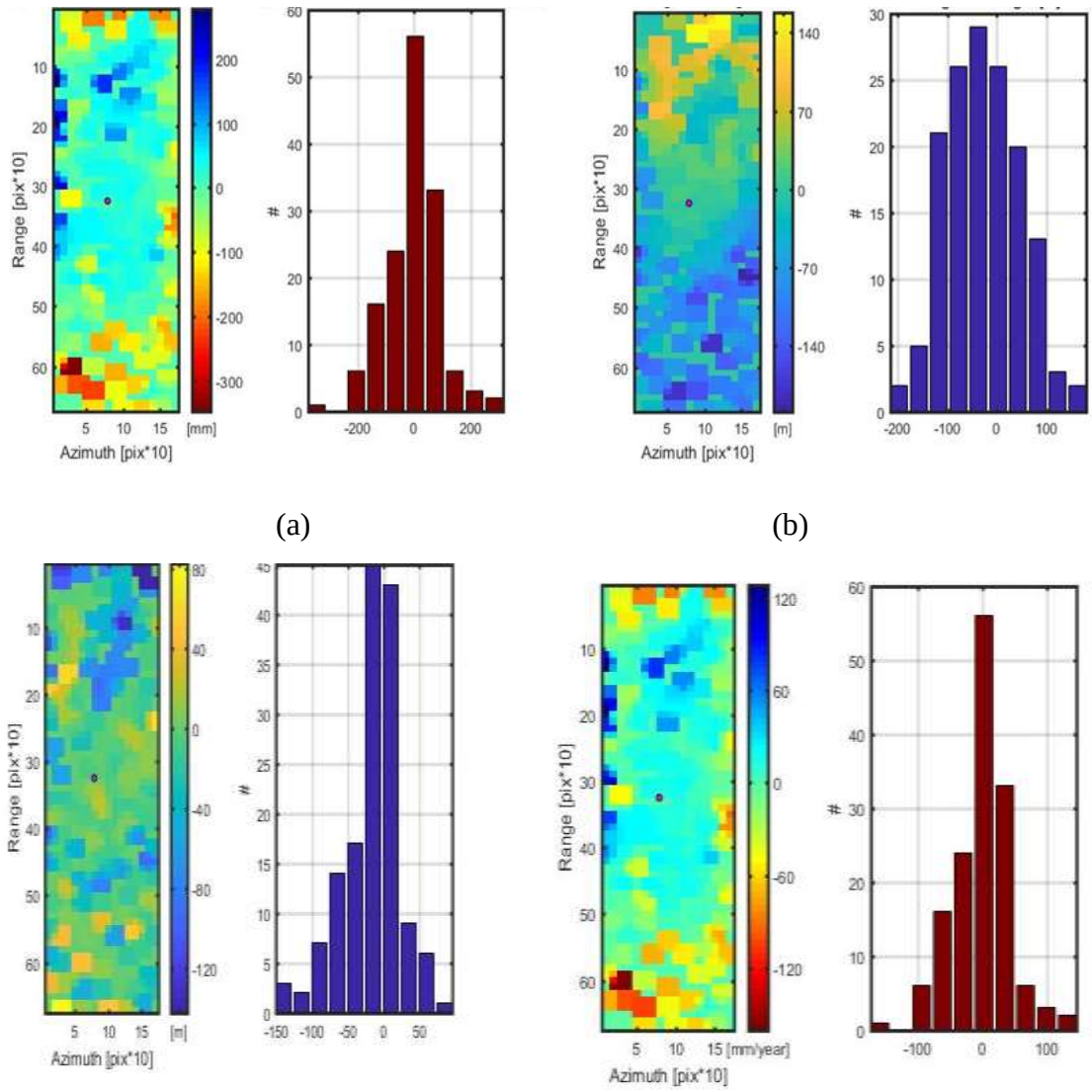


Figure 3.4 ASP Graph for reference point (a) Integrated Cumulative displacement, (b) Integrated Height, (c) Integrated Residual Height and (d) Integrated Velocity.

Following the removal of the APS, a second parameter estimation was done on a larger set of locations, which were chosen based on a spatial coherence and ASI combination criterion. All PS point with a good temporal coherence over a valid criterion (mainly based on the number of images studied in the data-stack and amplitude stability index) was selected at the end of the PS analysis

to map time series deformation. A linear deformation trend model was used to calculate the LOS velocity, displacement time series, and heights for each PS. The assumption in linear deformation modeling is that the target changes at a constant rate. The best way to see how velocities change over time is to look at the time series for each individual point.

As a result, a reference point among the possibilities expected to be stable is chosen, and the estimated ground velocities are relative to this presumed stable point. However, the choice of reference point is subjective because it is based on the user's judgment. Although the stable point can have certain starting velocities, they are presumed to be zero because its sole purpose is to serve as a reference velocity for other points. As a result, while deformation maps created by various users may appear to be different, they are supposed to be comparable in terms of relative quality. Because of the spatial closeness of the locations, atmospheric and noise are decreased in time series (Hooper et al., 2012).

Atmospheric artifacts are spatially but not temporally correlated, whereas deformation is both spatially and temporally correlated. This data is used to apply a filter in order to estimate atmospheric influences, which is the main benefit of the MT-InSAR technique. In the Figure 3.5 and Figure 3.6 the average annual subsidence of ground for each PS candidate is the ultimate outcome, assuming as a linear deformations.

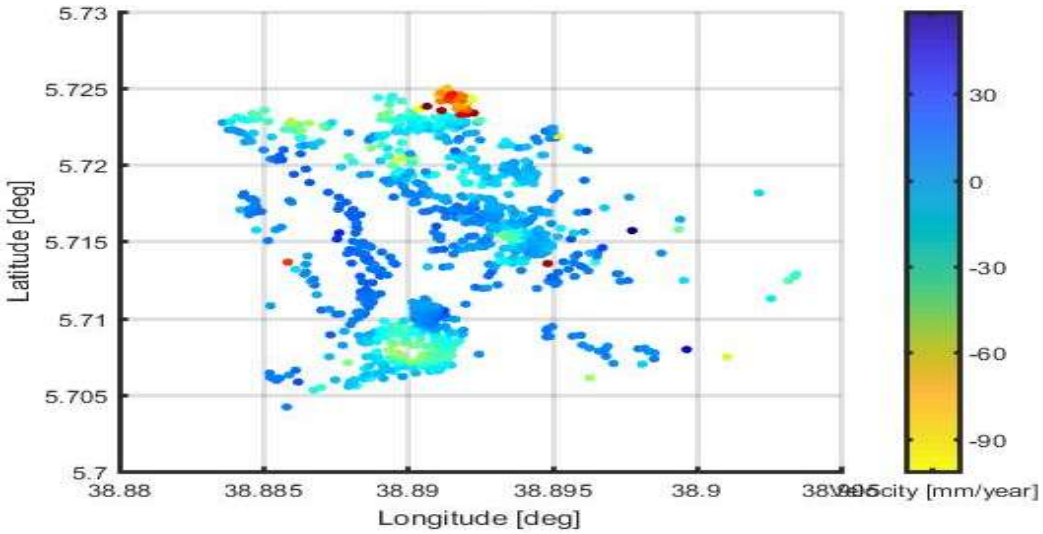


Figure 3.5. Scatter plot of PS Candidate of study area for Ascending sentinel image

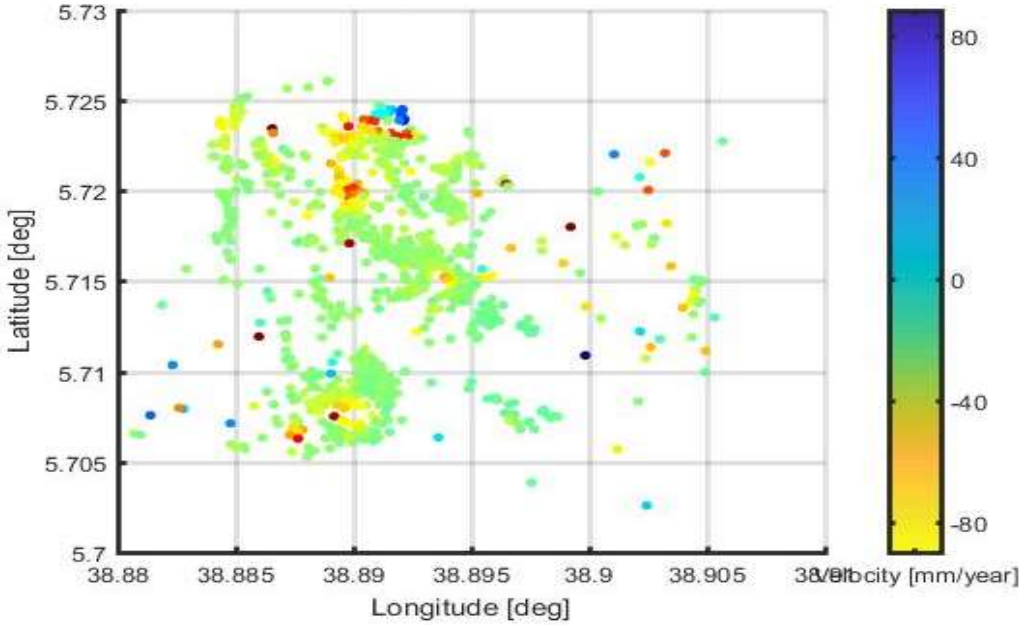


Figure 3.6. Scatter plot of PS candidate of Study area for Descending sentinel image

3.6. Normalized Difference Vegetation Index (NDVI)

Normalized difference vegetation Index (NDVI) quantifies vegetation by measuring the difference between near-infrared in which vegetation strongly reflects and red light in which vegetation absorbs. The values closer to +1 indicate that the area is covered by dense vegetation and the values closer to -1 indicate that the area is covered by water body. If the NDVI values closer to 0 or less implies that there is less or no vegetation in the area. In this study, the NDVI values was calculated from the SENTINEL 2A data set as follows:

$$NDVI = \frac{B8-B4}{B8+B4} \quad (5)$$

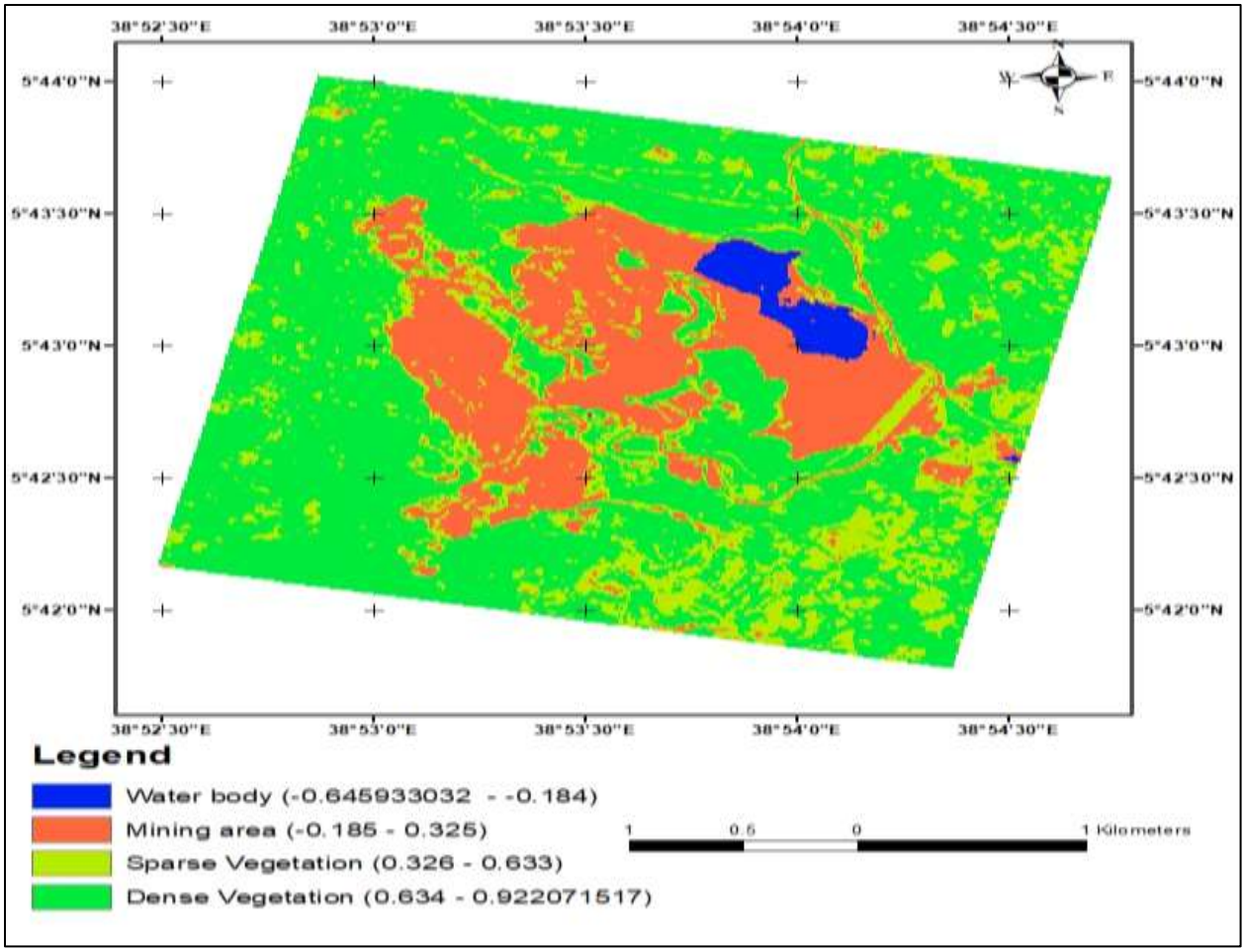


Figure 3.7. Normalized difference vegetation index map of the study area

3.7.Validation Method

3.7.1. Regression Analysis

In regression analysis, the regression approach is used to find a link between these two interdependent variables based on a large number of observations. The most widely used model is linear regression, which is defined as:

$$Y=mx+c \quad (6)$$

So, this regression method was also used to validate the ground deformation between InSAR and ground survey measurements. M and C are the unknown parameters, x and y are two known variables. In this validation, x is the ground survey displacement value, while y is the displacement value retrieved using InSAR. The correlation coefficient and the root mean square error (RMSE) are two parameters used to assess the accuracy of a regression analysis. The degree of fit between

the regression model and the observations is described by the correlation coefficient, with a value approaching 1 indicating a closer fit. Select 30 measurements throughout the validation site for these two variables' validation, which implies that for each year of Ground survey data, select one displacement value per year based on the InSAR measurement with the same year and month.

3.8. General Methodological workflow of the Study

The implementation of SARPROZ for PS processing is used in the conceptual workflow for persistent scatterer in InSAR deformation analysis. The processes taken to process the InSAR (SENTINEL-1A) data from 2014-2016 years are depicted in Figure 3.8. To achieve the goal in the intended InSAR data processing, 52 radar images with distinct timestamp that completely cover the study area were selected. The initial step was export SLC data with its contents and selected the sub swaths of the exported SLC image to break the images into the required sub swaths. Then, using an orbit file operator, precise satellite position and velocity information may be obtained.

After that, the best master image was selected. The reference master image was selected to have the lowest amount of spatial (m) and temporal (days) baseline. Furthermore, it was chosen in such a way that it maximizes the interferometric stack's predicted coherence. The selection of an "ideal" reference also improves in the visual interpretation of interferograms and the production of high-quality findings. A single-reference-stack is created with the specified reference image, in which all secondary images are co-registered to the reference image.

After co-registration apply; the next steps are processing for reflectivity and amplitude stability index calculation, selection of GCP and external DEM, APS processing, PS selection and APS estimation is followed. To reduce the atmospheric phase delay effect, the calculated APS is eliminated from the differential interferograms. Following the elimination of the APS, the final phase of SPS processing is performed on the PSs network to provide a final estimate of height and line of sight (LOS) velocity for the development of a cumulative displacement map over the PS points.

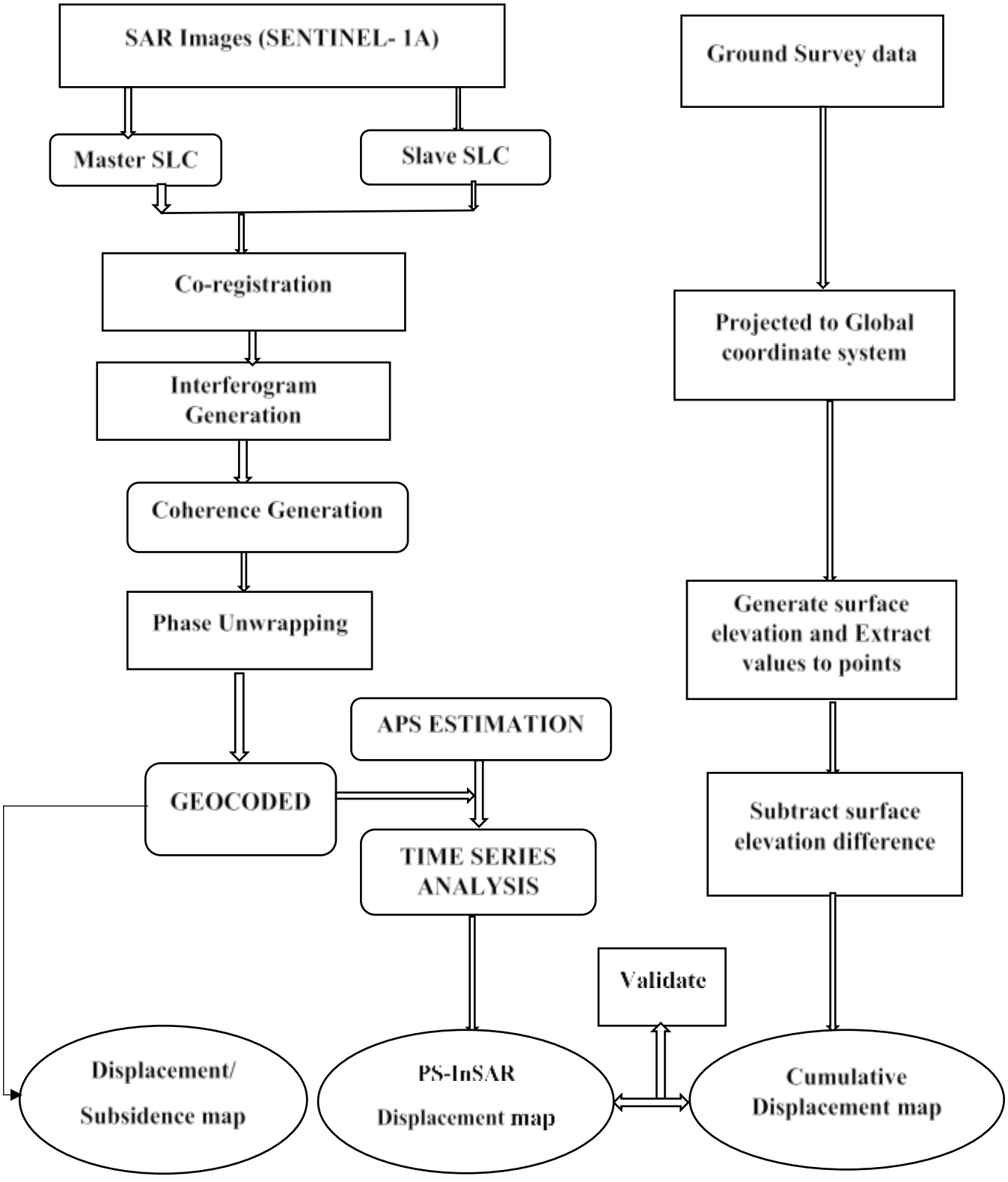


Figure 3.8 Conceptual frame work of data processing.

CHAPTER 4

4. RESULTS AND DISCUSSION

The ground surface displacement velocity map is extracted using the interferogram and InSAR time-series results to highlight the major deformation behavior in the area of line of sight. The displacement velocity map contains the subsidence rate along the LOS direction. Use the one band of SAR data, namely C-band Sentinel dataset. Have a number of dataset of C-band, 52 of sentinel data period gathered over the period ranging from 2014 to 2016. These datasets were evaluated using Persistent Scatters and single interferogram methods was developed to investigate deformation of the ground surface in open pit mining and surrounding area. Results of sentinel dataset illustrated deformation patterns of the study area. Besides, vertical deformations of the mining site were determined using InSAR method using sentinel datasets. The subsidence rate was estimated as several millimeters per year using the stacking method. First, SLC SAR datasets were processed in pre-processing software packages. The SLC dataset were extracted to my study area of 20 km to 1km. The second step was co-registration; Co-registration means that for each image, the resolution cells of the same geographic place are overlaid. This is done using precise orbital information. After completing the co-registration of slave images to their respective master image, a multi-look ratio finished of 5:5 (final pixel size 25 m by 25 m) were used to generate raw interferograms and subsequent products for the next step. The mean and resampled surface displacement velocity map is extracted under the assumption of infinite flattering. Therefore, any non-linear deformation, including atmospheric artefacts, has been damped out. The displacement maps are generated using the deformation sequences acquired from the PS time series analysis, which span the same time intervals as the interferograms. The artefacts commonly assumed to be atmospheric are greatly reduced in the resulting subsidence maps, demonstrating the smoothing effect. The velocity map allows for the identification of the long term subsidence. However, the main strength of the time series analysis in PS-InSAR techniques is; it's potential to detect deformation signals that are not steady in time, including seasonal effects of the study area. To evaluate the results of the time-series analysis, take ground survey measurements which are a continuously measured by survey section of mining company with the same years interval in InSAR measurement.

The generated interferogram phase contains orbital errors, topographic effects, target displacements and atmospheric noise. Orbital errors, topography effects, and atmospheric noise were eliminated from the interferogram in order to obtain the accurate ground surface displacement over a defined time interval in the study area. For the topographic effect removal the SRTM DEM with the spatial resolution of 30m were used. Refer to an appendix part that Figure A.1 show the interferometric configuration of ascending dataset as a graph describing the relationship between the images in function of time and perpendicular baseline. Each image is connected to the selected Master image, forming an interferometric pair.

4.1. Resampled displacement

The interferograms were then unwrapped, and adaptive filter was applied to each differential interferograms to reduce phase noise and improve subsequent 2D phase unwrapping. These interferograms provide the relative displacement along the radar line of sight (LOS) direction. Further processing of the InSAR data allows us to estimate deformation velocity for each interferogram derived from Sentinel -1A satellite missions (i.e. Sentinel from 2014-2016). The deformation rates in the Line of Sight of the Persistent Scatter points determined by processing the ascending and descending datasets are shown in Figure 4.3and Figure 4.4 respectively.

Midroc lega dembi Gold mine subsidence in the direction away from the satellite LOS at a resampled displacement ranging from 160mm to -160 mm as computed from Sentinel -1A data of Ascending Geometries as showed in Figure 4.1. The same data but Descending Geometry also showed the resampled subsidence of the study area towards the satellite at a rate of 140 to −140 mm as showed in Figure 4.2. Zero rate of displacement represents an almost stable area; where deformation is not significantly going on. To evaluate the second dataset, another interferometric pair of Sentinel images, was selected, the vertical displacement rates of a few millimeters per year was observed in small areas of the stacked interferogram that are contrasted by broader regions of several centimeters of displacement observed in some short term single pair interferogram. Positive values indicate a movement of the object toward the sensor (uplift), while negative values indicate the opposite (subsidence).

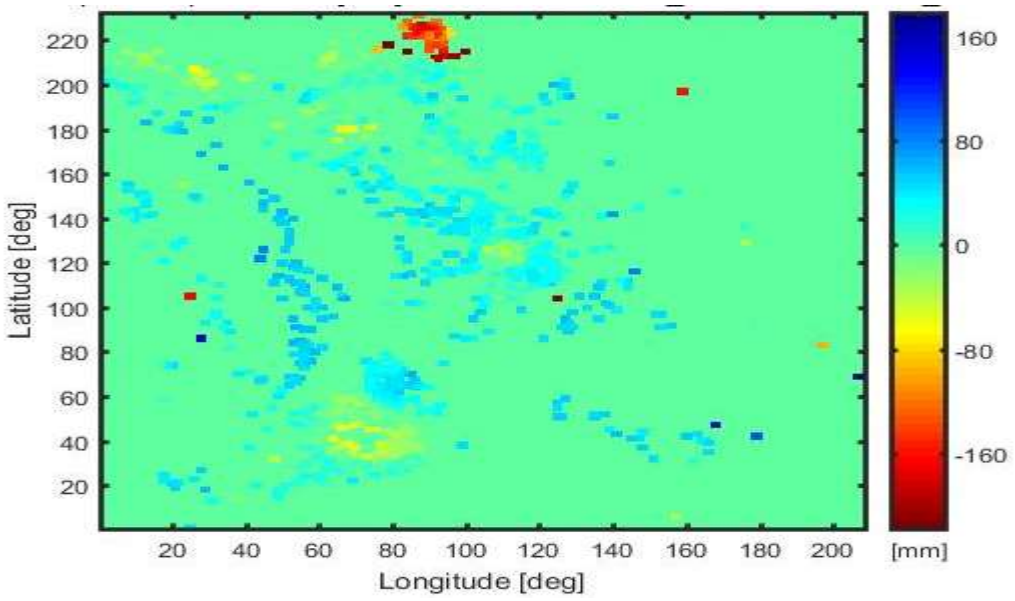


Figure 4.1 Resampled Displacement of study area for ascending sentinel-1A images

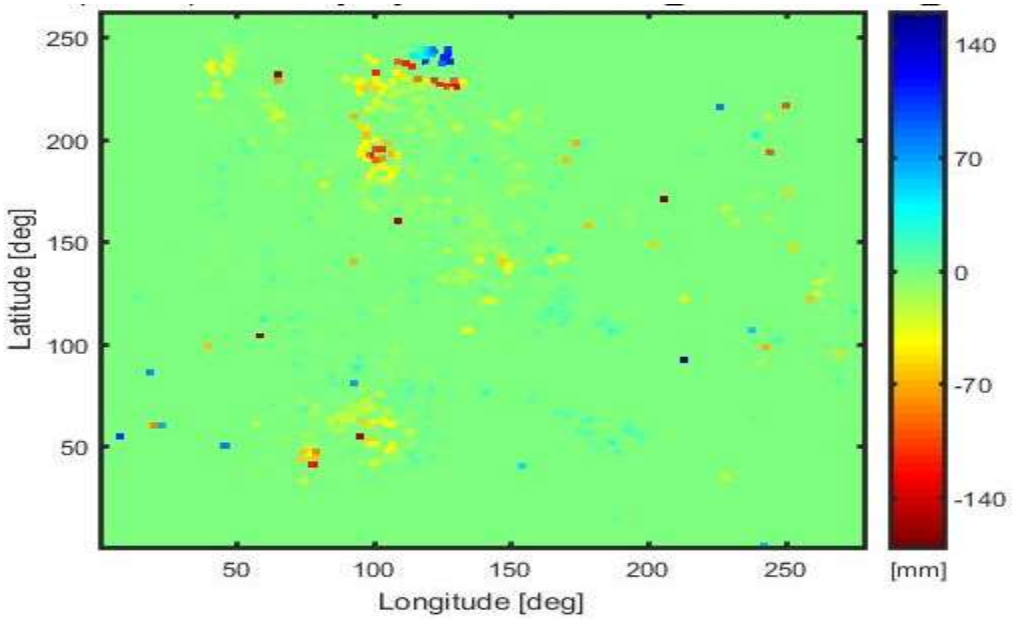


Figure 4.2 Resampled Displacement of study area for descending Sentinel -1A images

Due to the difference in temporal resolutions among different radar datasets, the rate of subsidence determined from each data source across the study area showed slight variability. The maximum rates of observed resampled deformations are: −160 and −140 mm from sentinel ascending and descending data respectively as showed in Figure 4.1 and Figure 4.2. The velocity map shows the spatial variability of deformation across the study area. Large Ascending interferograms detected ground subsidence, with observed some uplift showed in Figure 4.3. For example, significant

subsidence (maximum 90 mm) and uplift (maximum 30 mm) are observed in the satellite LOS direction as recovered from the Ascending image. The Descending imageries showed uplift (maximum 80 mm) and subsidence (maximum 80 mm) in the LOS direction. From the deformation rate-maps, the identify features of the deformation field that are evident in both Ascending and Descending InSAR datasets. In this study, the Ascending interferogram result shows that; the values of ground subsidence in the satellite LOS direction larger than the descending interferogram results. This is due to the looking direction and the incidence angle of the sensitivity vector and the geometry of the fault which means displacement vector. Verifying the application of Sentinel-1A with independent evidence from another radar data set and also providing more information about a greater temporally extent of the deformation field in the mining area was classify the observed displacements into two categories according to the magnitude and temporal extent of the deformation. These are: (1) less temporal extent have low magnitude (up to -80mm) relative subsidence labelled in Figure 4.3; (2) relative cumulative subsidence of -100 mm/yr. was observed at the midroc lega Dembi gold site.

4.2. Cumulative Displacement by InSAR

The PS value of sentinel-1A data almost covers the central, northern and southern parts of Midroc lega dembi Gold mine, showing more availability of ground surface deformation and some ground surface uplift. The rate of deformation relative to the resample displacement of sentinel -1A data is almost the same across the study area. However, it exhibits slight spatial variability red, light blue and blue points indicating subsidence, stable targets and uplift, respectively

In sentinel dataset the PS value covers all mining activities and in some extent cover infrastructure areas. PS numbers derived from sentinel -1A data set are less in number, indicating that the area of midroc lega dembi gold mining are non-linear ground surface deformation and the area of mining activities covered in very dense vegetation.

Each point of the PS method indicates deformation rate of specific waste dump area, underground and open pit mining area, road and any other man made infrastructure. So the PS rate shows more blue, blue and light blue color it means light blue is zero or no deformation at the central and western part of the midroc lega Dembi gold mine and red color at northern part indicating maximum deformation, the light red shows minimum rate deformation at the southern and some part of north-west in mining area.

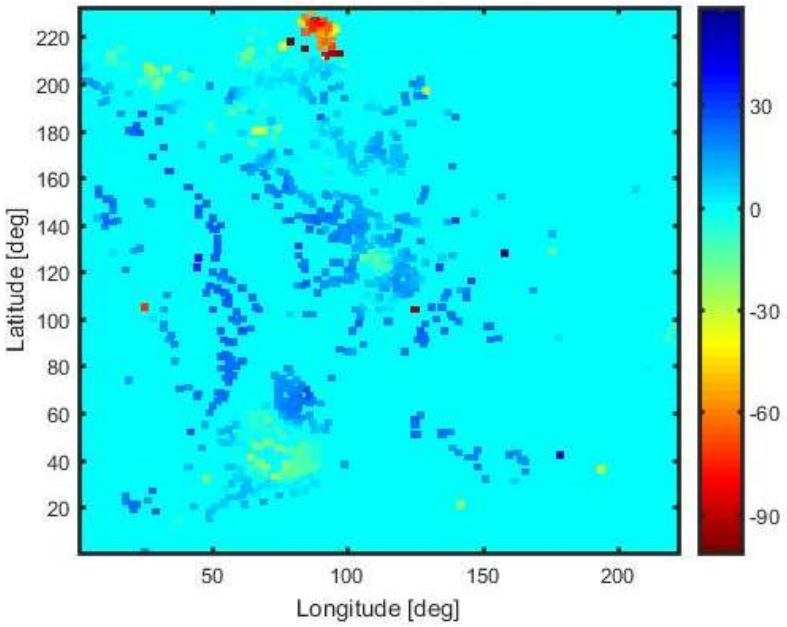


Figure 4.3 Resampled velocity of study area for Ascending Sentinel -1A images

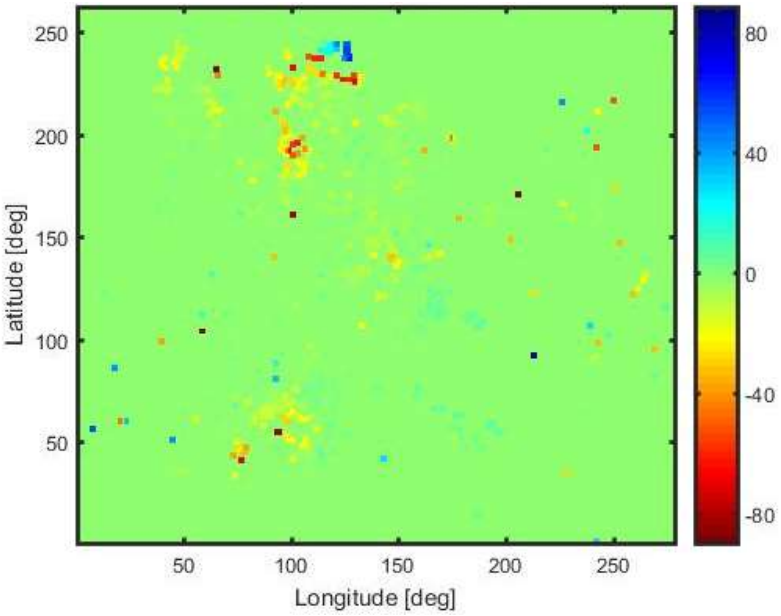


Figure 4.4 Resampled Velocity of study area for Descending Sentinel -1A images

For example; in the Figure 4.3 showed different results compared to the Figure 4.4. But these ascending data sets and Descending data set have the same sub swath and area coverage and in Figure 4.3 the PS values are very disperse all over the study area. More stable areas are described by light blue color and ground surface deformation is maximum in the northern and southern parts of the mining activities area (as indicated by red points). PS value colored by light blue showed

more stable areas while red and light red values reflect deformation in northern and south region of the midroc lega dembi gold mine. InSAR derived ground surface deformation rates and displacements are also validated using an independent estimates derived from ground survey data, located at midroc lega Dembi gold mine. In some area InSAR based PS ground surface displacements and time series ground survey measurements are the same (zero level displacement). This indicates that the ground survey data of that point are stable area. In this work, PSI analysis Figure 4.5 showed that waste dump area, closed gold site and underground mining area are the most critical and unstable area. Besides, extensive dormant mass movements and consequently characterized by the highest PSI ground motion rates were observed across this study area.

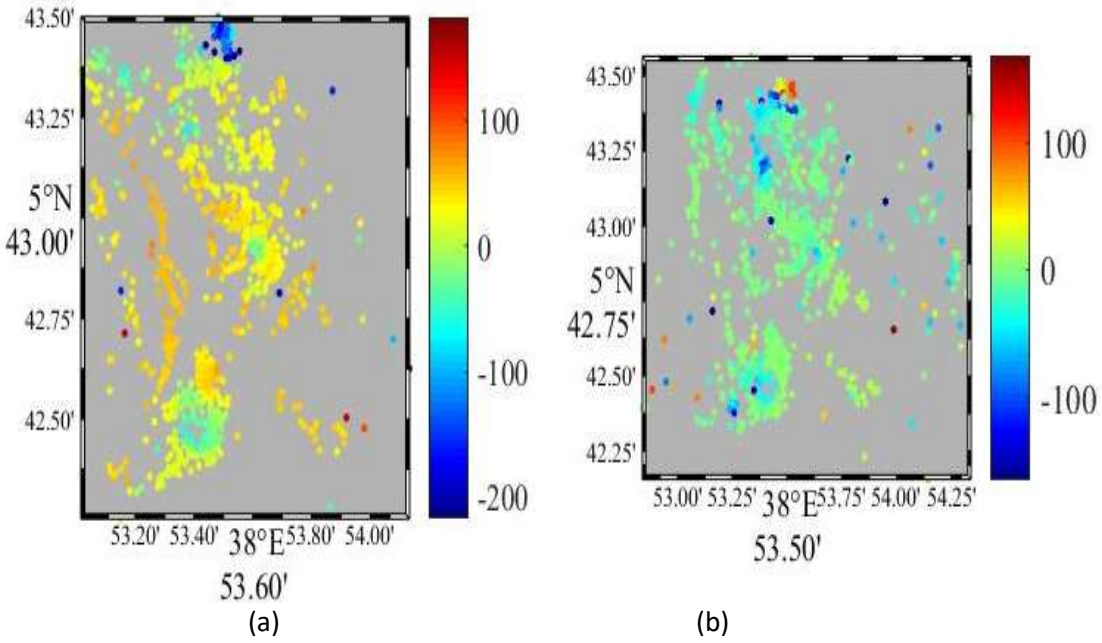


Figure 4.5 Cumulative displacement map of Ascending SAR geomerty (a) and Descending SAR geometry(b) from the 2014-2016 of the study area.

4.3. **C**umulative displacement for the ground survey data

Ground survey data was collected by survey section of the mining company. This study uses 2014 to 2016 ground survey data which collected by survey section of the mining company to obtain cumulative displacement of the ground surface. The years of the observation for both the ground survey data and InSAR measurement was the same. The ground survey data collected by the mining company was in local coordinate system and it needs conversion to fit within InSAR

measurement. Matlab software and 2D projection parameters were used to convert this local coordinate system to UTM. By using the surface elevation values of converted ground survey data; extract point values for all PS points which generated by InSAR techniques within the study area extent for both years i.e. 2014 and 2016 respectively. To measure ground surface displacement from the ground survey data; the difference of two measured data i.e. 2014 ground survey data and 2016 ground survey data was calculated. The Figure 4.6 shows the surface difference of two ground survey measurements and cumulative displacement of −3.99866 and -0.00012207 m values was extract from Ground survey data of entire study area.

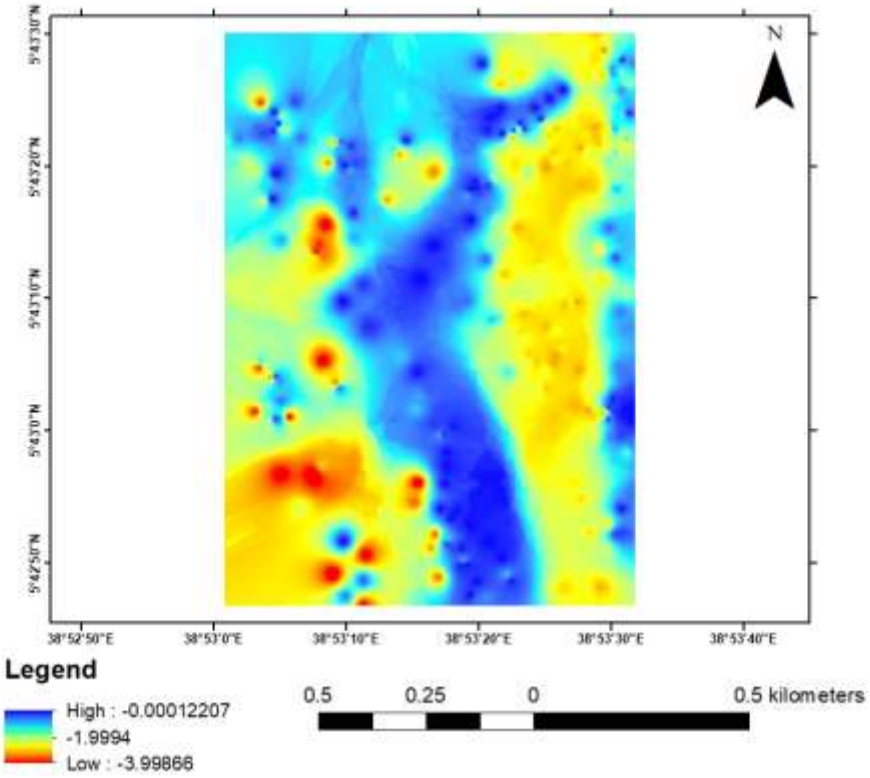


Figure 4.6 Cumulative Displacement of Ground survey data

4.4. Validation

The final analysis of the ground survey data yielded ground surface displacement results, which are presented in Appendix

Table B.5. For every year of the Ground survey data; there are both cumulative displacements measured from Ground survey data and the displacement extracted from InSAR data. They were compared using LOS regression by using linear regression equation. Regression result between InSAR and Ground Survey data displacement of the at Midroc Lega Dembi open pit mine were showed in Figure 4.7. The x-axis represents displacement from Ground survey data, and the y-axis indicates displacement estimated by InSAR. The red line represents the linear regression result. The linear correlation coefficient value r is 0.98 which means positive correlation and relative to close to the constant of 1, implying that the fit between InSAR measurements and ground survey data is very high, meaning closely to the monitoring result of selected point. An analysis of the RMSE is 3.24, a value significantly very larger than 1 indicating that the difference between InSAR measurement and ground survey data are large to show ground surface deformation.

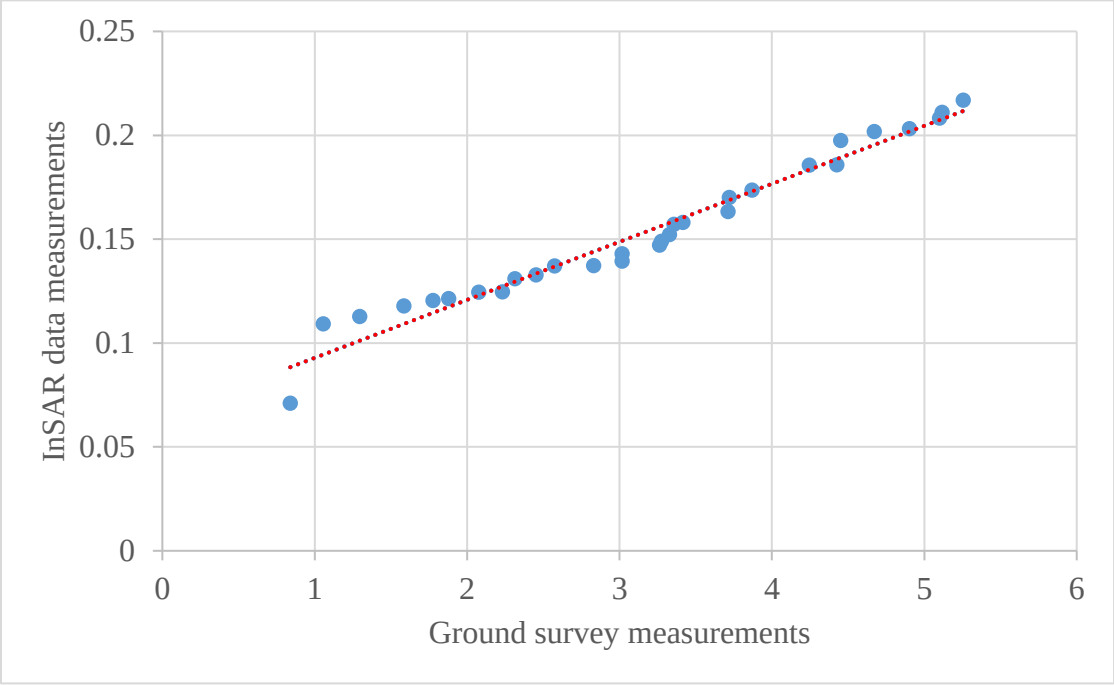


Figure 4.7 Validation of InSAR measurements and Ground survey measurements

4.5. **DISCUSSION**

The overall objectives of the study was to evaluate the capability of using InSAR methods to monitor ground surface deformation around the study area by using Sentinel-1 SAR imagery and Ground survey data. With this, to measure and characterize land surface movements around the mine, evaluate the uncertainty in the measurements and compare the results of the PSI time series analysis with the ground survey data observations of the study area.

Surface deformation near the Midroc Lega Dembi Goldfields was measured successfully using PSI techniques and ground survey data from 2014 to 2016. It was expected that the most severe surface deformation would occur closest to the mining activity due to the large on-going topographic changes resulting from surface extraction. Although this is largely true in the observed deformation patterns, the most severe surface deformation rates are measured on the area of waste dump and in some part of the closed mining activity. In this study area, the deformation pattern were observed to the northern, southern and central part of the mining operations area. In other case, the active parts of the lega dembi mines are in the western portions of the mining pits, is actively excavating Gold from the western portion of the mine and the surface deformation rate is no observed in this area by InSAR techniques; however, the area is highly deformed as observed from ground survey data. Areas of heavy vegetation coverage tend to show moderate rates of surface uplift. This is likely caused by the vegetation canopies being the main source of scattering in these areas, rather than the soil surface below. As a result, the InSAR techniques are measuring the growth of a vegetation canopy and not the surface movement of the land surface. Due to dense vegetation and SAR geometry, more of the active open pit mining region and closed open pit parts of the study area experience little to no surface movement, and some parts of the built-up areas closest to the mines experiencing the corresponding surface subsidence.

There is no agreement of deformation directionality when comparing deformation measurements to in-situ survey data within the deformation determined using the InSAR technique, and this is the same when comparing with the study done by Mieszko Fydrych *et al.*, (2021) in Canada. The direction of surface movement, along the LoS, for PSI measurements are not the same for the area around the active open pit mine of the ground survey data. The direction of deformation measured by the PS-InSAR techniques only agree well with the Northern part of Open pit of the ground survey measurements, which are insignificant. The PSI results in this study reveal only small

surface uplift in the active open pit area throughout the years, but the Ground Survey data shows significant surface subsidence in the active open pit area and only small surface subsidence in the waste dump area and closed site. 30 points of InSAR measurements and ground survey measurements with the same locations and years were selected for validation. The correlation coefficients value of the ground surface subsidence rate obtained using PS technique and ground survey data was 0.98 in this selected point, which is consistent with Nassir, (2019) previous research findings on structural deformation in Ethiopia. The values tell that the subsidence value extract from InSAR method are strongly correlated with the values of obtained from ground survey data for selected point. The high RMSE values seen over agricultural/vegetation areas indicate substantial mistakes often related to atmospherics or unwrapping issues when compare with other studies by Simons, Fialko and Rivera, (2002); Mw7.1 Hector mine, in California. However, this expanded coverage provides extra information that may be utilized to fill in the gaps of PSI and in-situ measurements and provide a more comprehensive understanding of land deformation trends in the region and this issue is discussed by Pawluszek-Filipiak and Borkowski, (2020a); Rydułtowy Mine in Poland.

Many studies in different countries use different InSAR methods to monitor ground surface deformation in mining areas. Studies in India, New York, Sweden, China, Iraq, and Germany have used different InSAR techniques to monitor ground subsidence in mining areas, and the results have been compared to ground survey data or GNNS measurements. But in this particular study area; there is no InSAR and ground survey data based study practices to monitor ground surface deformation in mining activity area. Kumar et al., (2020a) and his colleagues focused their research on detecting continuous slow rate of ground subsidence in five key JCF locations in India. The maximum rate of gradual deformation across all locations was 29 mm/year, with a total subsidence value of 90 mm, and the study region included the building area and railway tracks. To compare the accuracy of the two methodologies, the validation of subsidence data produced using PS-InSAR is compared to the previously published report and the master plan of JCF. Another research conduct in New York; in Rock salt mine by Valentino, (2016) was generate InSAR time series by using a persistent scatterers approach for two independent overlapping tracks with data spanning the time period from 22 December, 2006 to 24 march, 2011. The results of InSAR time series was compared with the levelling data provided by the American Rock salt company and observe the maximum rates on order of 8cm/year in the near-vertical LOS direction, with a sign

consistent with subsidence. Furthermore, the researcher discovered that, despite the impact of dense vegetation and agriculture, the InSAR data quality is sufficient for resolving non-linear subsidence corresponding to the extension of mining activity over time and when compared to this study it happened the same impact of dense vegetation, the researcher's results were relatively similar to this study.

Similar studies have been done on ground surface subsidence due to coal mining in area of south of Leipzig in German by Haghighi and Motagh, (2017). In this study, time series of Sentinel-1A data are analyzed by using the Small Baseline Subset (SBAS) approach provides new insights into mining-induced deformations in the study area and the results shows rapid subsidence of up to 4cm/year between October 2014 and April 2017 in two active open pit mining areas of the study area. Du *et al.*, (2021) used the SBAS-InSAR technique to gather three years surface subsidence information from sentinel-1A SLC products, covering a mining area in an Alpine Mining in the Tianshan Mountains, china and the subsidence cumulative was compared with field GNSS observation findings to verify its accuracy. With a maximum subsidence rate of -44.80mm/year and a maximum uplift rate of 28.04mm/year, the study region subsides significantly as a researcher analysis. Over a three-year period, the maximum subsidence and cumulative subsidence of the entire study region were -129.39mm and 60.49mm, respectively.

CHAPTER FIVE

5. CONCLUSION AND RECOMMENDATIONS

5.1. Conclusion

Ground surface deformation is one of the most essential issues when assessing safety and environmental impacts of open pit and underground mines area. Due to the logistical issues commonly present with traditional monitoring techniques, remote sensing solutions have become increasingly popular to handle such tasks. These ground surface deformation were measured in the midroc lega Dembi Goldmine in shakiso, by using sentinel -1A data from 2014-2016 and Ground survey data. In this study the InSAR technique was used in order to detect the ground surface deformation in the Midroc Lega Dembi caused by land subsidence due to mining operations. In this thesis the first finding of the significance of the study was discovery to monitoring ground surface deformation in that area of mining operations and in order to achieve this finding of the significance; produce 56 interferogram for ascending SAR image and 50 interferogram for Descending SAR image which collected from 2014 to 2016 were analyzed respectively.

Although the study area is surrounded dominantly by vegetation and forest covered, the InSAR techniques was unable to observe the center of the open pit which is the large mine-induced surface deformation within sufficient number of PS points. A zone of major ground surface deformation were detected in southern, Northern and some Eastern parts of Midroc lega dembi Gold mine was observed by using PSI. In this study area, a nonlinear behavior of deformation was detected from times series analysis of selected points. The results show that PSI method contributes to identify significant improvement for the monitoring of mining subsidence over dense vegetation mining areas likes Midroc Lega Dembi gold mine.

Furthermore, detailed ground surveying data and measurements of the ground water table would be helpful to the external validation process. Because the mining operations include non-coherent processes, repeat-pass monostatic DInSAR observations over the area provide issues in terms of decorrelation and phase ambiguity. This problem could be solved by using single-pass InSAR data, such as TanDEM-X, which would allow for higher height and spatial resolutions as well as better coverage of the research area. The results of PS-InSAR deformation measurements over the Midroc Lega Dembi Gold mine reveal that InSAR techniques may be used to monitor large-scale

mining-induced surface changes. In comparison to traditional monitoring approaches, these techniques provide a cost-effective and labor-intensive option for measuring surface displacements in difficult-to-reach places. Traditional monitoring approaches, which have limited spatial and temporal coverage, can also be used to fill in the measurement gaps with InSAR measurements. Finally, the PS-InSAR technique has a good potential to analysis the land subsidence in mining area; if that mining operation area have a less vegetation and built-up and the multi-temporal analysis of C-band data with adopted methodology is practically feasible for measuring, monitoring, and mapping of the slow rate of surface subsidence in mineral mining areas.

5.2. Recommendations

To achieve an accurate ground surface deformation monitoring, further work needs to be focused on expanding the collection of in-situ measurements indicated above, as well as increasing the number of SAR scenes used (such as Sentinel-1, Sentinel-2, and Sentinel-3), (TerraSAR-X and COSMO Sky-Med, which are not free of charge, but they would give a higher quality to the results.) as well as the establishment of a broad GNSS network to characterize extensive surface deformation. Ground water data of the study area cannot be used to supplement in-situ measurements in this study. This would provide insight on the connection between ground surface displacements and excessive ground water extraction during mining activities. If they have this information, together with specific overburden extraction rates, would provide for a better understanding of the relationship between mining production and regional subsidence, as well as insight into mine geotechnical concerns and this type of data were needs consideration in mining industry study.

The capabilities and limitations of InSAR techniques are highlighted in this study. However, while there is a requirement for less field effort on another hand, the area characteristics limit the quality of the results on the other (e.g. vegetation covered area) and to overcome this limitation the researchers were analyzed more number of images with the extended time period of observations and apply in area which have less vegetation particularly for urban and built-up area. Additionally, InSAR is unable to provide direct information on processes that occur within the mining ground, such as internal collapse or faults in the mining region and to obtain the accurate of the ground surface subsidence rate in mining area; any SAR (sentinel-1A) data user should be used the ground

survey measurement and clearly interpret the geological pattern of the study area to manage the environmental and nearby infrastructure damage.

Further research was continue to monitor mineral mining-related deformation in both rural and urbanized areas for hazard management using the methodologies described in this study and also by using the additional geodetic approaches such as geophysical investigation, and field inventories.

References

Abdikan, S., Mrikan, M., Sanli, F. and Cakir, Z. (2014) 'Monitoring of coal mining subsidence in peri-urban area of Zonguldak city (NW Turkey) with persistent scatterer interferometry using ALOS-PALSAR', *Environmental Earth Sciences*, 71(9), pp. 4081–4089. doi: 10.1007/s12665-013-2793-1.

Adamu, W. K. (2018) 'School of Graduate Studies School of Earth Sciences Geology , Geochemistry and Genesis of Ula Ulo Nickel Deposit , Adola Belt , Southern Ethiopia School of Graduate Studies School of Earth Sciences Geology , Geochemistry and Genesis of Ula Ulo Nickel Depo'.

Aimaiti, Y., Yamazaki, F. and Liu, W. (2018) 'Multi-sensor InSAR analysis of progressive land subsidence over the coastal city of Urayasu, Japan', *Remote Sensing*, 10(8). doi: 10.3390/RS10081304.

Alfarrah, N. and Walraevens, K. (2018) 'Groundwater overexploitation and seawater intrusion in coastal areas of arid and semi-arid regions', *Water (Switzerland)*, 10(2). doi: 10.3390/w10020143.

Anderssohn, J., Motagh, M., Walter, T.R., Rosenau, M., Kaufmann, H. and Oncken, O. (2009) 'Surface deformation time series and source modeling for a volcanic complex system based on satellite wide swath and image mode interferometry: The Lazufre system, central Andes', *Remote Sensing of Environment*, 113(10), pp. 2062–2075. doi: 10.1016/j.rse.2009.05.004.

Askne, J. I. H., Fransson, J.E.S., Santoro, M., Soja,M.J. and Ulander, L.M.H.J. (2013) 'Model-based biomass estimation of a hemi-boreal forest from multitemporal tanDEM-X acquisitions', *Remote Sensing*, 5(11), pp. 5574–5597. doi: 10.3390/rs5115574.

Bamler, R. and Hartl, P. (1998) 'Note the " errata " (correction of some small errors) on the last page ! Synthetic aperture radar interferometry', 14(September), pp. 1–55.

Berardino, P., Fornaro, G., Lanari, R. and Sansosti, E. (2002) 'A new algorithm for surface deformation monitoring based on small baseline differential SAR interferograms', *IEEE Transactions on Geoscience and Remote Sensing*, 40(11), pp. 2375–2383. doi: 10.1109/TGRS.2002.803792.

Billay, A. Y., Kisters, A.F.M., Meyer, FM. and Schneider, J. (1997) 'The geology of the Lega Dembi gold deposit, southern Ethiopia: Implications for Pan-African gold exploration', *Mineralium Deposita*, 32(5), pp. 491–504. doi: 10.1007/s001260050117.

Borghero, C. (2017) 'Feasibility study of dam deformation monitoring in northern Sweden using

Sentinel1 SAR interferometry', p. 77.

Bountzouklis, C. (2016) 'Monitoring of Santorini (Greece) volcano during post-unrest period (2014-2016) with Interferometric Time series of Sentinel-1A', (404).

Bu, R., Rosen, P. A. and Fielding, E. J. (2000) 'Synthetic aperture radar interferometry to measure earth's surface topography and its', pp. 169–209.

Calais, E., Freed, A., Mattioli, G., Amelung, F., Jonsson, S., Jansma, P., Hong, S., Dixon, T., Prepetit, C. and Momplaisir, R. (2010) 'Transpressional rupture of an unmapped fault during the 2010 Haiti earthquake', *Nature Geoscience*, 3(11), pp. 794–799. doi: 10.1038/ngeo992.

Casu, F., Mancani, A., Pepe, A. and Lanari, R. (2011) 'Deformation time-series generation in areas characterized by large displacement dynamics: The SAR amplitude pixel-offset SBAS technique', *IEEE Transactions on Geoscience and Remote Sensing*, 49(7), pp. 2752–2763. doi: 10.1109/TGRS.2010.2104325.

Celik, H. K., Rennie, A. E. W. and Akinci, I. (2011) 'Deformation behaviour simulation of an apple under drop case by finite element method', *Journal of Food Engineering*, 104(2), pp. 293–298. doi: 10.1016/j.jfoodeng.2010.12.020.

Cloude, S. R. (2009) 'Polarized point scatterers: An algorithm for detection using ALOS-PALSAR data', *International Geoscience and Remote Sensing Symposium (IGARSS)*, 5, pp. 150–153. doi: 10.1109/IGARSS.2009.5417709.

Crosetto, M., Monserrat, O., Cuevas-Gonzalez, M., Devanthery, N. and Crippa, B. (2016) 'Persistent Scatterer Interferometry: A review', *ISPRS Journal of Photogrammetry and Remote Sensing*, 115, pp. 78–89. doi: 10.1016/j.isprsjprs.2015.10.011.

Du, Q., Li, G., Zhou, Y., Chai, M., Chen, D., Qi, S. and Wu, G. (2021) 'Deformation Monitoring in an Alpine Mining Area in the Tianshan Mountains Based on SBAS-InSAR Technology', *Advances in Materials Science and Engineering*, 2021. doi: 10.1155/2021/9988017.

Duro, J., Albiol, D., Mora, O. and Payas, B. (2013) 'Application of advanced InSAR techniques for the measurement of vertical and horizontal ground motion in longwall minings', *13th Coal Operators' Conference, University of Wollongong, The Australasian Institute of Mining and Metallurgy & Mine Managers Association of Australia*, pp. 99–106.

ESA (2015) *ESA's Optical High-Resolution Mission for GMES Operational Services*.

Farr, T., Rosen, P., Caro, E., Crippen, R., Duren, R., Hensley, S., Kobrick, M., Paller, M., Rodriguez, E., Roth, L., Seal, D., Shatter, S., Shimada, J., Umland, J., Werner, M., Oskin, M.,

Burbank, D. and Alsdort, D. (2008) 'Shuttle Radar Topography Mission: Mission to map the world', *Reviews of Geophysics*, 45(2), pp. 3–5. doi: 10.1029/2005RG000183.1.Introduction.

Featherstone, W. (1998) 'Do we need a gravimetric geoid or a model of the Australian height datum to transform GPS heights in Australia?', *Australian Surveyor*, 43(4), pp. 273–280. doi: 10.1080/00050350.1998.10558758.

Ferretti, A., Monti-guarnieri, A., Prati, C., Rocca, F. and Massonnet, D. (2007) 'InSAR Principles: Guidelines for SAR Interferometry Processing and Interpretation', *ESA Publications*, (January), pp. 1–48.

Ferretti, A., Fumagalli, A., Novali, F., Prati, C., Rocca, F. and Rucci, A. (2011) 'A new algorithm for processing interferometric data-stacks: SqueeSAR', *IEEE Transactions on Geoscience and Remote Sensing*, 49(9), pp. 3460–3470. doi: 10.1109/TGRS.2011.2124465.

Ferretti, A., Prati, C. and Rocca, F. (2000) 'Nonlinear subsidence rate estimation using permanent scatterers in differential SAR interferometry', *IEEE Transactions on Geoscience and Remote Sensing*, 38(5 I), pp. 2202–2212. doi: 10.1109/36.868878.

Ferretti, A., Prati, C. and Rocca, F. (2001) 'Permanent scatterers in SAR interferometry', *IEEE Transactions on Geoscience and Remote Sensing*, 39(1), pp. 8–20. doi: 10.1109/36.898661.

Funning, G. J., Parsons, B., Wright, T.J., Jackson, J.A. and Fielding, E.J. (2005) 'Surface displacements and source parameters of the 2003 Bam (Iran) earthquake from Envisat advanced synthetic aperture radar imagery', *Journal of Geophysical Research: Solid Earth*, 110(9), pp. 1–23. doi: 10.1029/2004JB003338.

Gabriel, A. K., Goldstein, R. M. and Zebker, H. A. (1989) 'Mapping small elevation changes over large areas: differential radar interferometry', *Journal of Geophysical Research*, 94(B7), pp. 9183–9191. doi: 10.1029/JB094iB07p09183.

Galloway, D. L. and Burbey, T. J. (2011) 'Review: Regional land subsidence accompanying groundwater extraction', *Hydrogeology Journal*, 19(8), pp. 1459–1486. doi: 10.1007/s10040-011-0775-5.

Gascon, F. (2012) 'The Sentinel-2 mission products', *European Space Agency, (Special Publication) ESA SP*, 707 SP(March).

Getaneh, W. (1994) 'sulfide . mineralization in the lega dembi primary gold deposit , sidamo , A Thesis presented'.

Ghebreab, W., Gxoroxs, L. W. and Ababa, A. (1993) '/ U ~ X / U ~ V', 15(3), pp. 489–500.

Goldstein, R. M., Zebker, H. A. and Werner, C. L. (1988) 'Satellite radar interferometry: Two-dimensional phase unwrapping', *Radio Science*, 23(4), pp. 713–720. doi: 10.1029/RS023i004p00713.

Guéguen, Y., Deffontaines, B., Fruneau, B., Al Heib, M., de Michele, M., Raucoules, D., Guise, Y. and Planchenault, J. (2009) 'Monitoring residual mining subsidence of Nord/Pas-de-Calais coal basin from differential and Persistent Scatterer Interferometry (Northern France)', *Journal of Applied Geophysics*, 69(1), pp. 24–34. doi: 10.1016/j.jappgeo.2009.02.008.

Haghighi, M. H. and Motagh, M. (2017) 'Sentinel-1 InSAR over Germany: Large-scale interferometry, atmospheric effects, and ground deformation mapping', *ZFV - Zeitschrift fur Geodasie, Geoinformation und Landmanagement*, 142(4), pp. 245–256. doi: 10.12902/zfv-0174-2017.

He, Y., Wang, W., Yan, H., Zhang, L., Chen, Y. and Yang, S. (2020) 'Characteristics of surface deformation in lanzhou with sentinel-1a tops', *Geosciences (Switzerland)*, 10(3). doi: 10.3390/geosciences10030099.

Henderson, I. H. C., Lauknes, T. R., Osmundsen, P. T., Dehls, J., Larsen, Y. and Redfield, T. F. (2011) 'A structural, geomorphological and InSAR study of an active rock slope failure development', *Geological Society Special Publication*, 351(March 2011), pp. 185–199. doi: 10.1144/SP351.10.

Hooper, A., Zebker, H., Segall, P. and Kampes, B. (2004) 'A new method for measuring deformation on volcanoes and other natural terrains using InSAR persistent scatterers', *Geophysical Research Letters*, 31(23), pp. 1–5. doi: 10.1029/2004GL021737.

Hooper, A., Segall, P. and Zebker, H. (2007) 'Persistent scatterer interferometric synthetic aperture radar for crustal deformation analysis, with application to Volcán Alcedo, Galápagos', *Journal of Geophysical Research: Solid Earth*, 112(7), pp. 1–21. doi: 10.1029/2006JB004763.

Huang, J. L., Deng, K. Z., Fan, H. D. and Yang, J. K. (2015) 'Application of surface deformation monitoring in mining area by the fusion of InSAR and laser scan data', *International Archives of the Photogrammetry, Remote Sensing and Spatial Information Sciences - ISPRS Archives*, 40(7W4), pp. 41–44. doi: 10.5194/isprsarchives-XL-7-W4-41-2015.

Javad, M., Zarch, E., Wickert, J. and Bookhagen, B. (2019) 'Ground Deformation Monitoring in Mining Areas on the Central Andean Plateau (Puna, Argentina) Using Sentinel-1 Data', (March).

Ji, L., Zhang, Y., Wang, Q., Xin, Y. and Li, J. (2016) 'Detecting land uplift associated with enhanced oil recovery using InSAR in the Karamay oil field, Xinjiang, China', *International Journal of Remote Sensing*, 37(7), pp. 1527–1540. doi: 10.1080/01431161.2016.1154222.

Kalkan, Y. (2002) 'Deformation Surveying', (June), p. 53.

Khakim, M. Y. N., Tsuji, T. and Matsuoka, T. (2013) 'Detection of localized surface uplift by differential SAR interferometry at the hangingstone oil sand field, Alberta, Canada', IEEE Journal of Selected Topics in Applied Earth Observations and Remote Sensing, 6(6), pp. 2344–2354. doi: 10.1109/JSTARS.2013.2254471.

Kumar, S., Kumar, D., Chaudhary, S., Singh, N. and Malik, K. (2020) 'Land subsidence mapping and monitoring using modified persistent scatterer interferometric synthetic aperture radar in Jharia Coalfield, India', *Journal of Earth System Science*, 129(1). doi: 10.1007/s12040-020-01413-0.

Langley, R. B., Teunissen, P. J. G. and Montenbruck, O. (2017) *Introduction to GNSS, Springer Handbooks*. doi: 10.1007/978-3-319-42928-1_1.

Lazecký, M., Jiránková, E. and Böhmová, D. (2010) 'Usage of InSAR techniques to detect and monitor terrain subsidence due to the mining activities', *GeoScience Engineering Volume LVI*, 2010(January), pp. 32–49.

Liu, P., Li, Z., Hoey, T., Kincal, C., Zhang, J., Zeng, Q. and Muller, J. (2012) 'Using advanced inSAR time series techniques to monitor landslide movements in Badong of the Three Gorges region, China', *International Journal of Applied Earth Observation and Geoinformation*, 21(1), pp. 253–264. doi: 10.1016/j.jag.2011.10.010.

Liu, Z. G., Bian, Z. F., Lei, S. G., Liu, D. L. and Sowter, A. (2014) 'Evaluation of PS-DInSAR technology for subsidence monitoring caused by repeated mining in mountainous area', Transactions of Nonferrous Metals Society of China (English Edition), 24(10), pp. 3309–3315. doi: 10.1016/S1003-6326(14)63471-3.

Di Martire, D., Iglesias, R., Monells, D., Centolanza, G., Sica, S., Ramondini, M., Pagano, L., Mallorquí, J. J.and Calcaterra, D. (2014) 'Comparison between Differential SAR interferometry and ground measurements data in the displacement monitoring of the earth-dam of Conza della Campania (Italy)', Remote Sensing of Environment, 148, pp. 58–69. doi: 10.1016/j.rse.2014.03.014.

Massonnet, D., Briole, P. and Arnaud, A. (1995) 'Deflation of Mount Etna monitored by

spaceborne radar interferometry', *Nature*, pp. 567–570. doi: 10.1038/375567a0.

Massonnet, D. and Feigl, K. L. (1998) 'Radar interferometry and its application to changes in the earth's surface', *Reviews of Geophysics*, 36(4), pp. 441–500. doi: 10.1029/97RG03139.

Measurements, E. M. D. *et al.* (2021) 'Evaluating Multi-Temporal DInSAR Measurements of Ground Surface Deformation Around the Rhenish Coalfields in Germany Using Sentinel-1 SAR Imagery Waterloo , Ontario , Canada , 2021'.

Nagel, N. B. (2001) 'Compaction and subsidence issues within the petroleum industry: From Wilmington to Ekofisk and beyond', *Physics and Chemistry of the Earth, Part A: Solid Earth and Geodesy*, 26(1–2), pp. 3–14. doi: 10.1016/S1464-1895(01)00015-1.

Nassir, W. (2019) 'Structural Deformation Monitoring In Urban Area Using'.

Paradella, W. R., Ferretti, A., Mura, J. C., Colombo, D., Gama, F. F., Tamburini, A., Santos, A. R., Novali, F., Galo, M. Camargo, P. O., Silva, A. Q., Silva, G. G., Silva, A. and Gomes, L. L. (2015) 'Mapping surface deformation in open pit iron mines of Carajás Province (Amazon Region) using an integrated SAR analysis', *Engineering Geology*, 193, pp. 61–78. doi: 10.1016/j.enggeo.2015.04.015.

Parcharidis, I., Foumelis, M., Benekos, G., Kourkouli, P., Stamatopoulos, C. and Stramondo, S. (2015) 'Time series synthetic aperture radar interferometry over the multispan cable-stayed Rio-Antirio Bridge (central Greece): achievements and constraints', *Journal of Applied Remote Sensing*, 9(1), p. 096082. doi: 10.1117/1.jrs.9.096082.

Pawluszek-Filipiak, K. and Borkowski, A. (2020a) 'Integration of DInSAR and SBAS techniques to determine mining-related deformations using Sentinel-1 data: The case study of rydultowy mine in Poland', *Remote Sensing*, 12(2). doi: 10.3390/rs12020242.

Pawluszek-Filipiak, K. and Borkowski, A. (2020b) 'Monitoring mining-induced subsidence by integrating differential radar interferometry and persistent scatterer techniques', *European Journal of Remote Sensing*, 00(00), pp. 1–13. doi: 10.1080/22797254.2020.1759455.

Perissin, D. and Rocca, F. (2006) 'High-accuracy urban DEM using permanent scatterers', IEEE Transactions on Geoscience and Remote Sensi*ng*, 44(11), pp. 3338–3347. doi: 10.1109/TGRS.2006.877754.

Perissin, D. and Wang, T. (2012) 'Repeat-pass SAR interferometry with partially coherent targets', IEEE Transactions on Geoscience and Remote Sensi*ng*, 50(1), pp. 271–280. doi: 10.1109/TGRS.2011.2160644.

Perissin, D., Wang, Z. and Wang, T. (2011) 'The SARPROZ InSAR tool for urban subsidence/manmade structure stability monitoring in China', 34th International Symposium on Remote Sensing of Environment - The GEOSS Era: Towards Operational Environmental Monitoring.

Prats-Iraola, P., Nannini, M., Scheiber, R., De Zan, F., Wollstadt, S., Minati, F., Vecchioli, F., Costantini, M., Borgstrom, S., De Martino, P., Siniscalchi, V., Walter, T., Foumelis, M. and Desnos, Y. (2015) 'Sentinel-1 assessment of the interferometric wide-swath mode', *International Geoscience and Remote Sensing Symposium (IGARSS)*, 2015-Novem(July), pp. 5248–5251. doi: 10.1109/IGARSS.2015.7327018.

Quincey, D. J., Luckman, A. and Benn, D. (2009) 'Quantification of Everest region glacier velocities between 1992 and 2002, using satellite radar interferometry and feature tracking', *Journal of Glaciology*, 55(192), pp. 596–606. doi: 10.3189/002214309789470987.

Raucoules, D., Le Mouélic, S., Carnec, C. and King, C. (2002) 'Urban subsidence in the city of Prato (Italy) monitored by satellite radar interferometry', *International Geoscience and Remote Sensing Symposium (IGARSS)*, 2(February), pp. 1225–1227. doi: 10.1109/igarss.2002.1025896.

Rignot, E., Mouginot, J. and Scheuchl, B. (2011) 'Ice flow of the antarctic ice sheet', *Science*, 333(6048), pp. 1427–1430. doi: 10.1126/science.1208336.

Robertson, J. O., Chilingar, G. V., Khilyuk, L. F. and Endres, B. (2012) 'The environmental aspects of oil and gas production subsidence', *Energy Sources, Part A: Recovery, Utilization and Environmental Effects*, 34(8), pp. 756–773. doi: 10.1080/15567030903058519.

Rosen, P. A. (2000) 'Synthetic aperture radar interferometry', *Proceedings of the IEEE*, 88(3), pp. 333–380. doi: 10.1109/5.838084.

Ruiz-Armenteros, A. M., Bakon, M., Lazecky, M., Delgado, J. M., Sousa, J. J., Perissin, D. and Caro-Cuenca, M. (2016) 'Multi-Temporal InSAR Processing Comparison in Presence of High Topography', *Procedia Computer Science*, 100, pp. 1181–1190. doi: 10.1016/j.procs.2016.09.278.

Erol , S., Erol, B., T. A. (2002) 'A general review of the deformation monitoring techniques and a case study : Analysing deformations using GPS / levelling, ITU journal, Civil Engineering Faculty, Geodesy Division, 34469 Maslak Istanbul, Turkey.', p. 1.

Sahu, P. and Lokhande, R. D. (2015) 'An Investigation of Sinkhole Subsidence and its Preventive Measures in Underground Coal Mining', *Procedia Earth and Planetary Science*, 11(December), pp. 63–75. doi: 10.1016/j.proeps.2015.06.009.

Shimizu, K., Ota, T., Mizoue, N. and Saito, H. (2020) 'Comparison of multi-temporal planetscope data with Landsat 8 and Sentinel-2 data for estimating airborne LiDAR derived canopy height in temperate forests', *Remote Sensing*, 12(11). doi: 10.3390/rs12111876.

Shirvany, R. (no date) 'Estimation of the degree if polarization in polarimetric SAR imagery'.

Simons, M., Fialko, Y. and Rivera, L. (2002) 'Coseismic deformation from the 1999 Mw 7.1 Hector Mine, California, earthquake as inferred from InSAR and GPS observations', Bulletin of the Seismological Society of America, 92(4), pp. 1390–1402. doi: 10.1785/0120000933.

Solaro, G. *et al.* (2010) 'Anatomy of an unstable volcano from InSAR: Multiple processes affecting flank instability at Mt. Etna, 1994-2008', Journal of Geophysical Research: Solid Earth, 115(10), pp. 1994–2008. doi: 10.1029/2009JB000820.

Sousa, J. J., Ruiz, A.M., Hanssen, R.F., Perski, Z., Bastos, L., Antonio, J. and Galindo-Zaldívar, J. (2008) 'PS-INSAR measurement of ground subsidence in Granada area (Betic Cordillera, Spain)', Proceedings of the 13th FIG International Symposium on Deformation Measurements and Analysis, Lisbon, Portugal, (May), pp. 1–10.

Strozzi, T., Tosi, L., Carbognin, L., Wegmüller, U. and Galgaro, A. (2000) 'Monitoring Land Subsidence in the Euganean Geothermal Basin with Differential SAR Interferometry', *European Space Agency, (Special Publication) ESA SP*, (478), pp. 167–176.

Strozzi, T., Luckman, A., Murray, T., Wegmüller, U. and Werner, C. L. (2002) 'Glacier motion estimation using SAR offset-tracking procedures', IEEE Transactions on Geoscience and Remote Sensing, 40(11), pp. 2384–2391. doi: 10.1109/TGRS.2002.805079.

Strozzi, T., Kouraev, A., Wiesmann, A., Wegmüller, U., Sharov, A. and Werner, C. (2008) 'Estimation of Arctic glacier motion with satellite L-band SAR data', Remote Sensing of Environment, 112(3), pp. 636–645. doi: 10.1016/j.rse.2007.06.007.

Sund, M., Lauknes, T. R. and Eiken, T. (2014) 'Surge dynamics in the nathorstbreen glacier system, Svalbard', *Cryosphere*, 8(2), pp. 623–638. doi: 10.5194/tc-8-623-2014.

Tadesse, S. (1999) 'Geology and Gold Mineralization in the Pan-African Rocks of the Adola Area, Southern Ethiopia', *Gondwana Research*, 2(3), pp. 439–447. doi: 10.1016/S1342-937X(05)70282-3.

Tang, W., Motagh, M. and Zhan, W. (2020) 'Monitoring active open-pit mine stability in the Rhenish coalfields of Germany using a coherence-based SBAS method', *International Journal of Applied Earth Observation and Geoinformation*, 93(August), p. 102217. doi:

10.1016/j.jag.2020.102217.

Team, S. 2 E. (2015) 'Colour Vision for Copernicus', *Http://Esamultimedia.Esa.Int/*. Available at: http://esamultimedia.esa.int/multimedia/publications/ESA-Bulletin-161/offline/download.pdf.

Thapa, S., Chatterjee, R. S., Singh, K. B. and Kumar, D. (2016) 'Land subsidence monitoring using ps-insar technique for l-band sar data', *The International Archives of the Photogrammetry, Remote Sensing and Spatial Information Sciences*, XLI-B7(October), pp. 995–997. doi: 10.5194/isprs-archives-xli-b7-995-2016.

Tosi, L., Carbognin, L., Teatini, P., Strozzi, T. and Wegmüller, U. (2002) 'Evidence of the present relative land stability of Venice, Italy, from land, sea, and space observations', *Geophysical Research Letters*, 29(12), pp. 3-1-3–4. doi: 10.1029/2001GL013211.

Valentino, B. R. (2016) 'Application of insar to salt mine subsidence', (August).

Wang, Y., Guo, Y., Hu, S., Li, Y., Wang, J., Liu, X. and Wang, L. (2019) 'Ground deformation analysis using InSAR and backpropagation prediction with influencing factors in Erhai Region, China', *Sustainability (Switzerland)*, 11(10). doi: 10.3390/su11102853.

Wegmüller, U., Strozzi, T. and Tosi, L. (2000) 'ERS and ENVISAT differential SAR interferometry for subsidence monitoring', *European Space Agency, (Special Publication) ESA SP*, (461), pp. 203–210.

Werner, C., Wegmüller, U., Strozzi, T. and Wiesmann, A. (2003) 'Interferometric Point Target Analysis for Deformation Mapping', *International Geoscience and Remote Sensing Symposium (IGARSS)*, 7(1), pp. 4362–4364. doi: 10.1109/igarss.2003.1295516.

Wube, A. (2005) 'Mineralization and associated structures of Okote prospect', *Addis Ababa University, MSc Thesis*, p. 212. Available at: http://etd.aau.edu.et/bitstream/handle/123456789/4471.

Yang, Z., Li, Z., Zhu, J., Wang, Y. and Wu, L. (2020) 'Use of SAR/InSAR in Mining Deformation Monitoring, Parameter Inversion, and Forward Predictions: A Review', *IEEE Geoscience and Remote Sensing Magazine*, 8(1), pp. 71–90. doi: 10.1109/MGRS.2019.2954824.

Yi, S., Wang, Q. and Sun, W. (2016) 'Journal of Geophysical Research : Solid Earth', *Journal of Geophysical Research: Solid Earth*, pp. 3782–3803. doi: 10.1002/2015JB012608.Received.

Zhang, T., Shen, W., Wu, W., Zhang, B. and Pan, Y. (2019) 'Recent surface deformation in the Tianjin area revealed by Sentinel-1A data', *Remote Sensing*, 11(2), pp. 1–25. doi: 10.3390/rs11020130.

APPENDICES

Appendix A: Figures

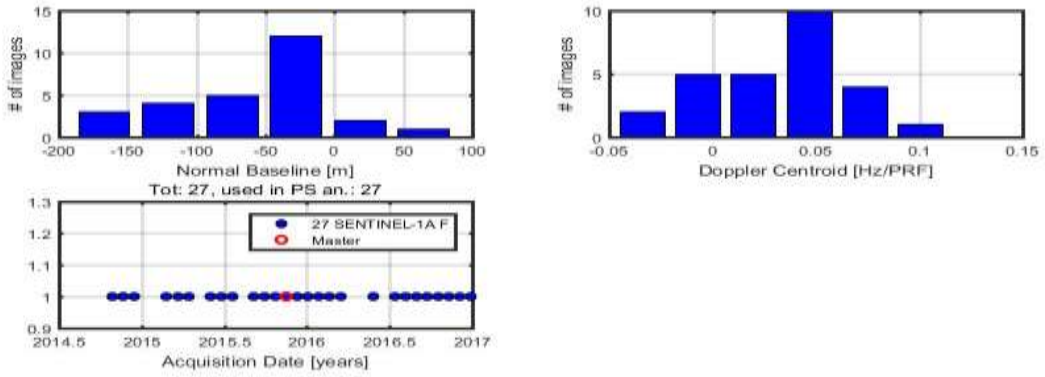


Figure A.1 Data statistics for sentinel -1A ascending data sets.

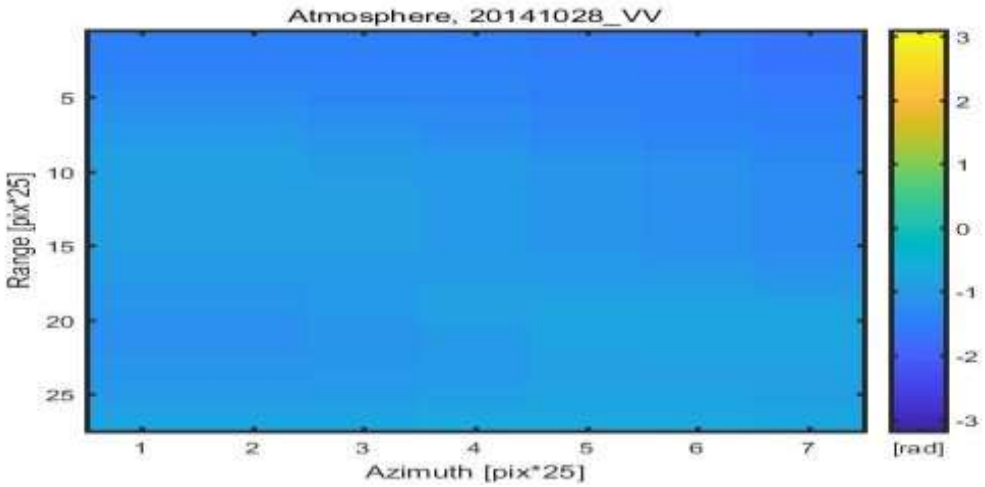


Figure A.2 Atmosphere of reference point.

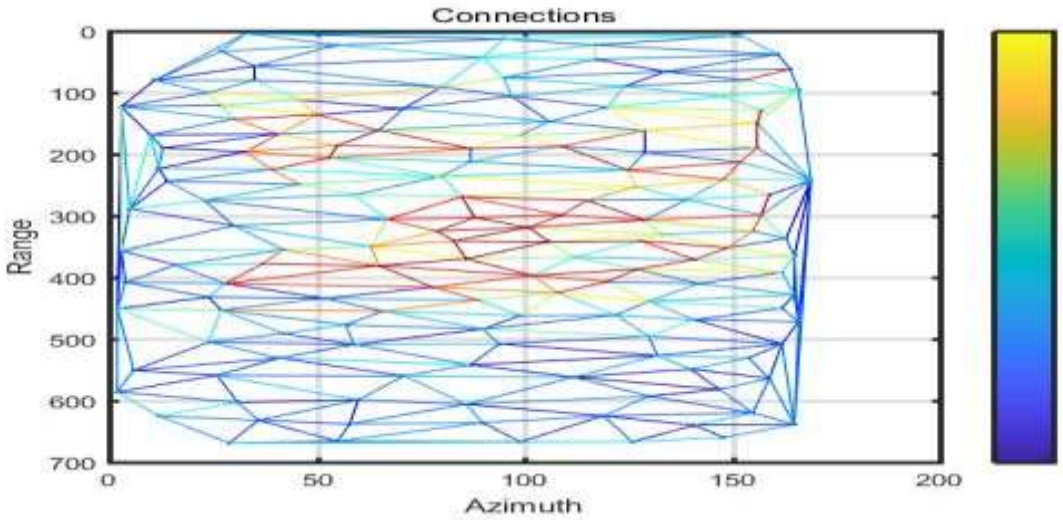


Figure A.3 Delaunay graph of sentinel-1A for ascending data set

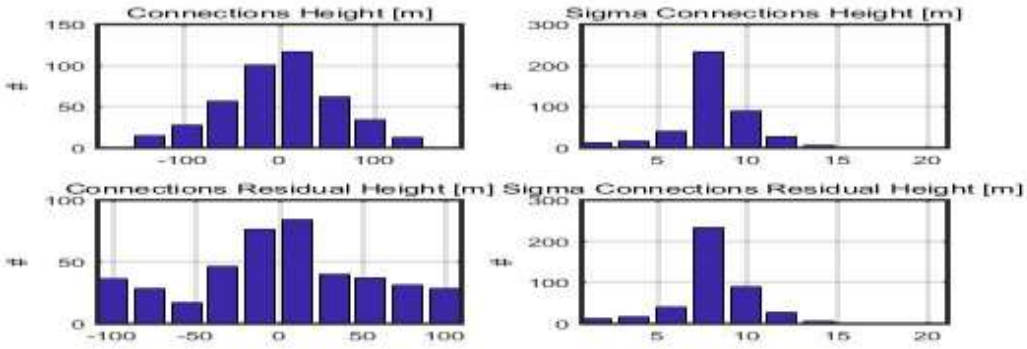


Figure A.4 APS removal in study area of connection height, sigma connection height, connection residual height, and sigma connections residual height

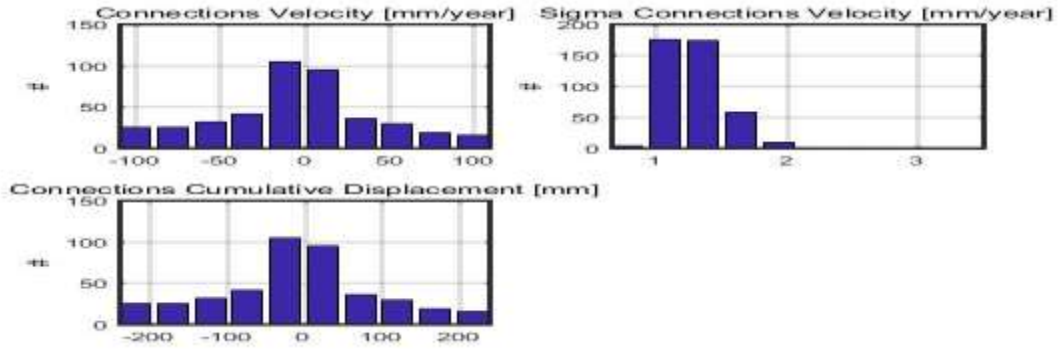


Figure A.5 APS removal in study area of connections velocity, sigma connections velocity, and connections cumulative Displacement

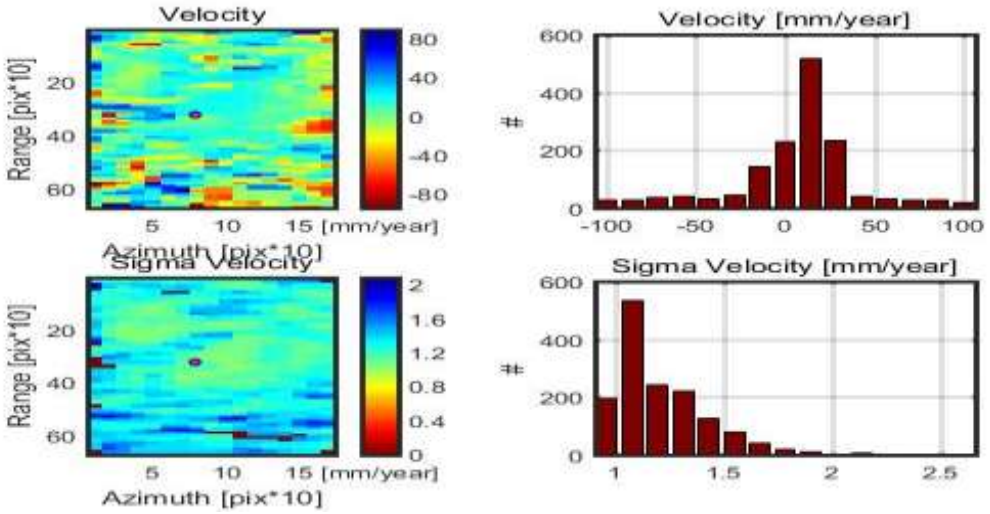


Figure A.6 APS removal of the study area for the velocity and sigma velocity

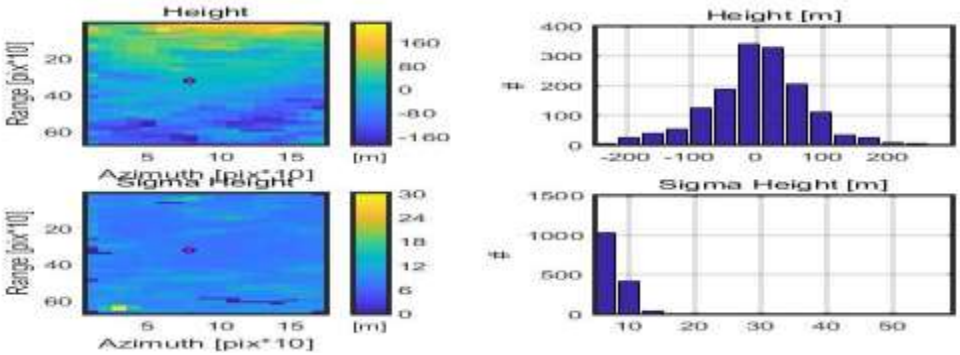


Figure A.7 APS removal of the study area for the height and sigma height

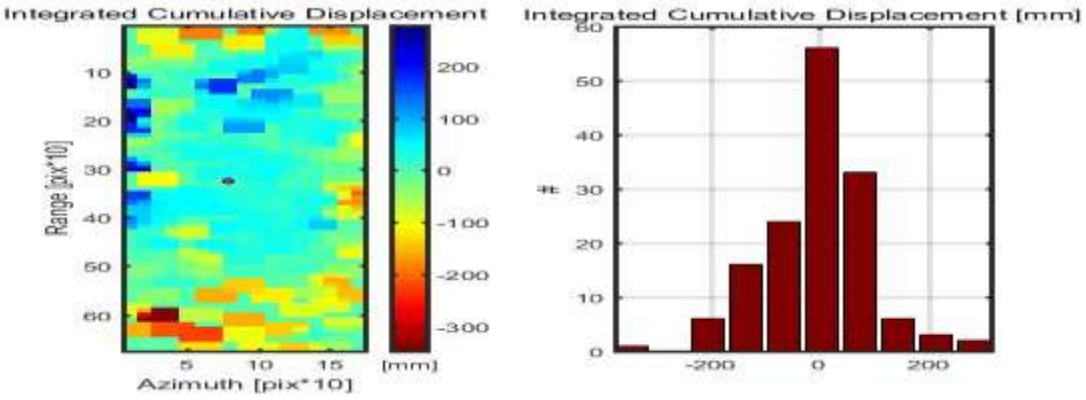


Figure A.8 APS removal of the study area for the integrated cumulative displacement

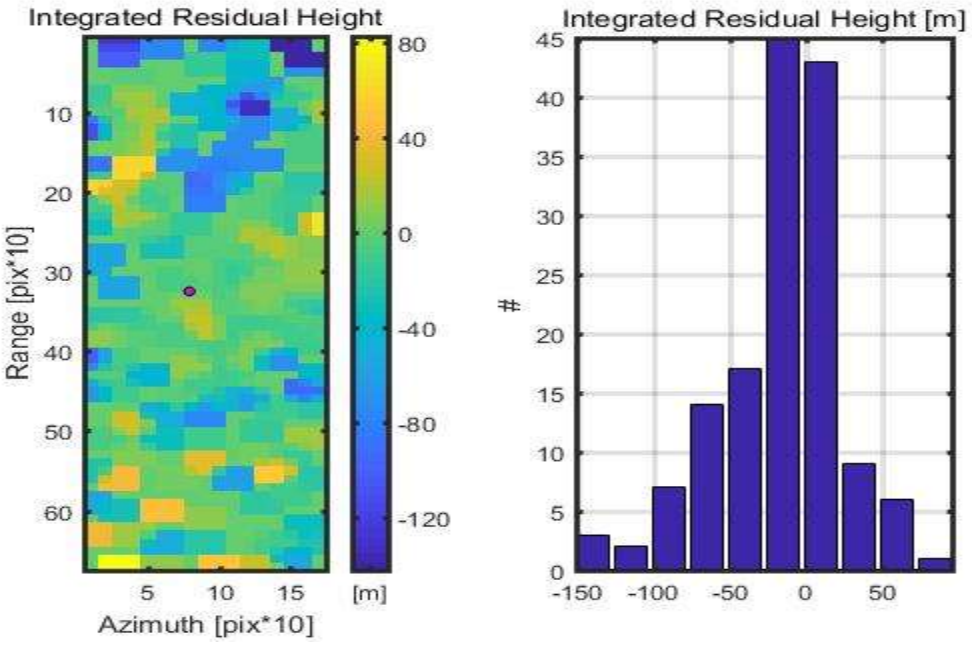


Figure A.9 APS removal of the study area for the integrated residual height

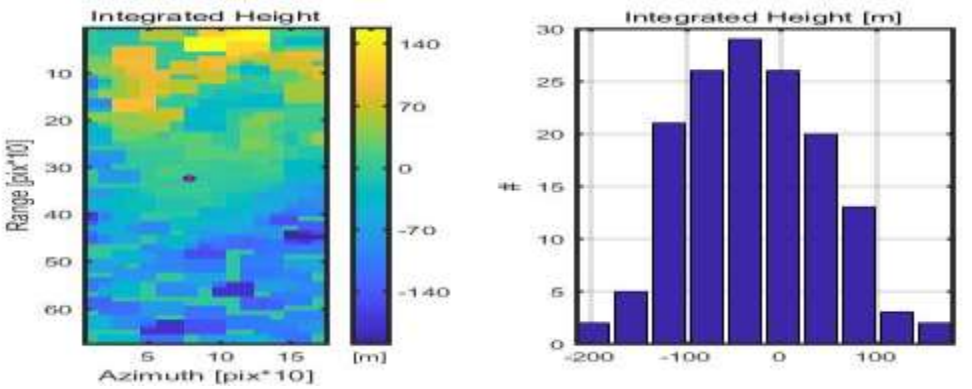


Figure A.10 APS removal of the study area for the integrated height.

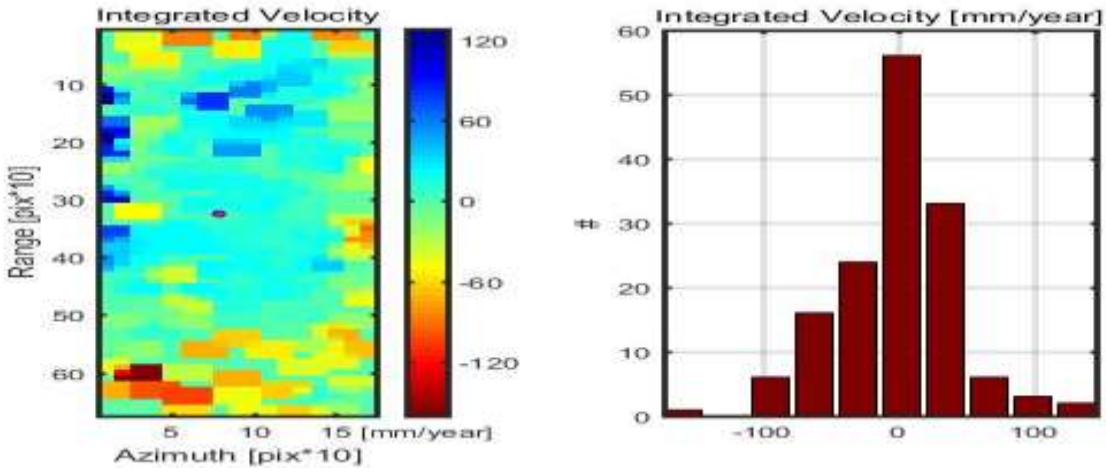


Figure A.11 APS removal of the study area for the integrated velocity.

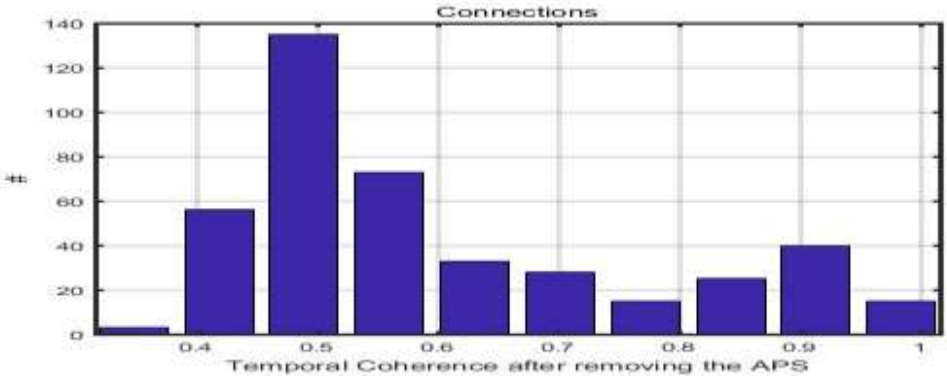


Figure A.12 Temporal Coherence after removing the APS.

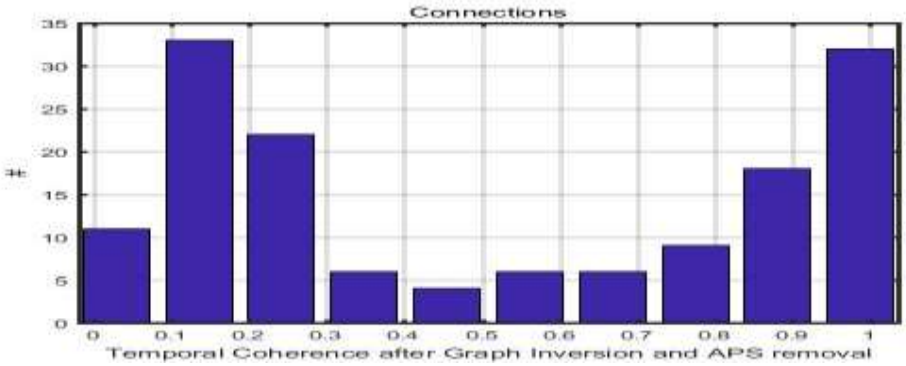


Figure A.13 Temporal coherence after Graph Inversion and APS removal.

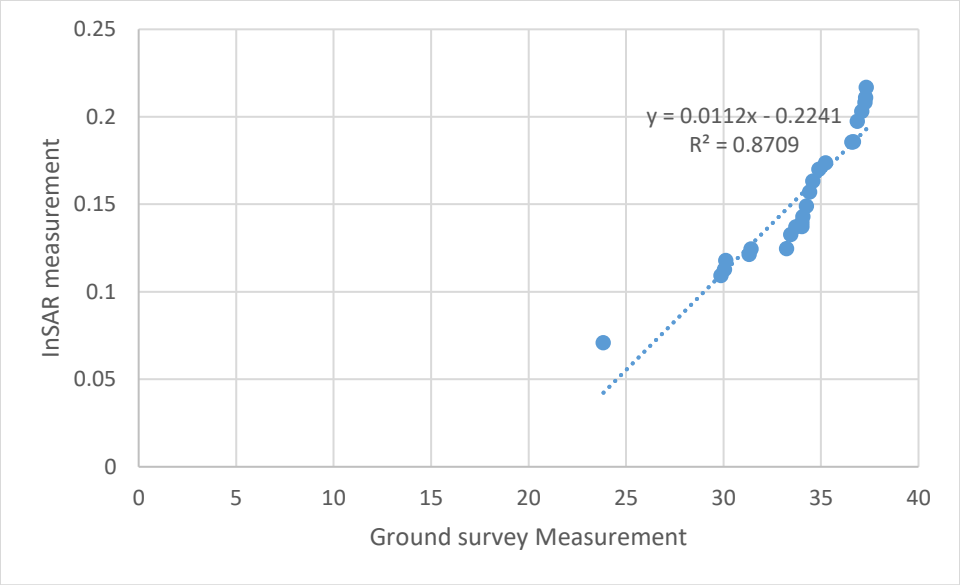


Figure A.14 Selected result validation point

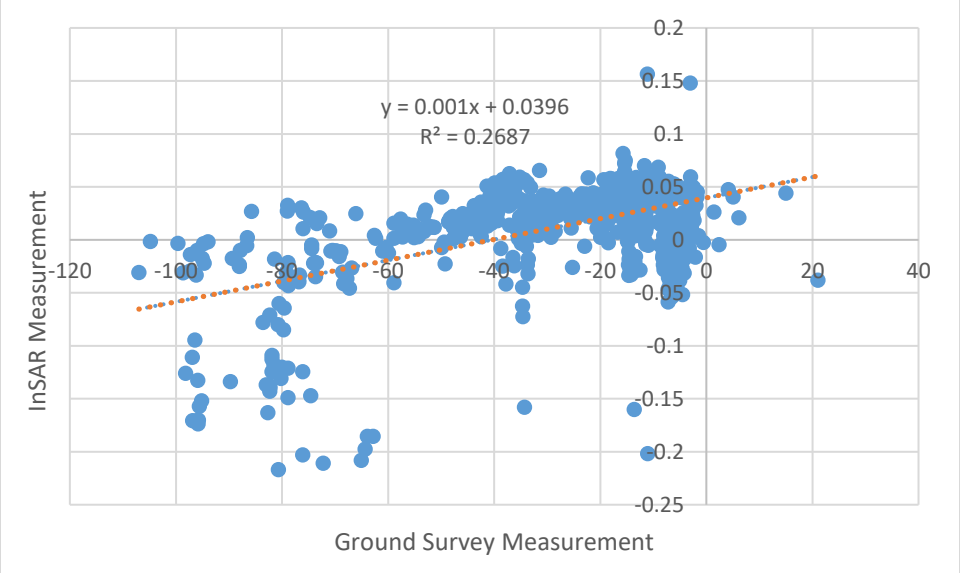


Figure A.15 Full data result validation points.

Appendix B: Tables

Table B.1 Local coordinate system ground survey data measurement of 2014

Northing	Easting	Elevation	Descrp
5996.766	5361.732	1959.562	Bh
5971.65	5371.223	1959.476	Bh
5980.467	5398.782	1960.157	Bh
5924.717	5417.333	1959.629	Bh
5919.697	5409.416	1958.775	Bh
5911.893	5393.393	1959.074	Bh
5910.376	5391.2	1959.831	Bh
5851.577	5410.504	1960.227	Bh
6050.644	5394.754	1959.068	Bh
5915.064	5485.951	1958.787	Bh
5595.609	5502.118	1950.453	Bh
5614.95	5537.681	1949.306	Bh
5374.616	5847.754	2028.57	
5381.704	5789.232	2021.108	
5487.734	5715.29	2009.448	
5546.813	5629.947	1998.645	
5572.725	5606.713	1994.035	
5677.815	5611.884	1984.11	
5681.421	5613.09	1983.765	
5739.663	5606.926	1979.243	
5836.272	5563.344	1968.287	
6094.816	5368.624	1960.29	
6099.028	5316.767	1970.538	
6053.663	5322.394	1969.318	
5988.176	5346.605	1971.016	
5756.56	5409.428	1961.992	
5517.856	5519.341	1961.143	
5196.059	5997.48	2047.466	

Table B.2 Local coordinates system Ground survey data measurement of 2016

Northing	Easting	Elevation	Description
5700.843	5522.133	1937.918	Borehole
5700.082	5508.91	1939.525	Borehole
5698.275	5493.493	1938.416	borehole
5698.378	5477.764	1938.61	borehole
5695.782	5455.726	1939.119	borehole
5694.912	5430.816	1941.408	borehole
5739.063	5520.402	1940.305	borehole
5739.829	5485.052	1939.178	borehole
5749.797	5432.579	1941.447	borehole
6013.735	5408.177	1949.514	borehole

6001.958	5365.04	1950.546	borehole
5964.754	5377.19	1949.769	borehole
6090.594	5353.719	1950.01	borehole
6090.253	5332.538	1951.329	borehole
5725.841	5582.815	1979.973	Cr
5547.06	5529.62	1960.389	Cr
5686.668	5416.379	1961.071	Cr
5866.936	5401.131	1960.049	Cr
6090.587	5325.123	1961.248	Cr
6092.438	5324.435	1962.221	Cr
5940.595	5485.755	1980.61	Cr
5725.841	5582.815	1979.973	Cr
5364.698	5604.13	1920.013	Toe
5284.613	5633.315	1920.805	Toe
5287.339	5654.005	1929.078	Toe
5344.245	5640.446	1919.244	Toe
5370.971	5660.629	1919.208	Toe
5427.7	5612.404	1920.245	Toe
5435.189	5601.711	1919.815	Toe
5438.655	5598.214	1920.09	Toe

Table B.3 Projected local coordinates system to UTM Coordinates system of 2014 and 2016

2014			2016		
Northing	Easting	Elevation	Northing	Easting	Elevation
5.7047161	38.897743	1780.4	5.7247001	38.891138	1760.4
5.7042007	38.885804	1931.18	5.7247255	38.891891	1737.11
5.714785239	38.88860852	1937.918	5.7246509	38.891528	1762.84
5.714665698	38.88860165	1939.525	5.7245769	38.891798	1743.82
5.714526322	38.88858532	1938.416	5.7245728	38.891777	1763.58
5.714384126	38.88858626	1938.61	5.7245116	38.89148	1761.68
5.714184893	38.8885628	1939.119	5.7244991	38.891419	1771.13
5.713959696	38.88855495	1941.408	5.7244852	38.891351	1770.54
5.714769612	38.88895405	1940.305	5.7244695	38.891904	1748.89
5.714450035	38.88896099	1939.178	5.7242982	38.8917	1753.81
5.713975665	38.88905113	1941.447	5.7242446	38.891439	1771.19
5.71375521	38.89143725	1949.514	5.7241965	38.891205	1763.17
5.713365229	38.8913308	1950.546	5.724182	38.891135	1762.29
5.713475048	38.89099446	1949.769	5.7242093	38.891896	1758.61
5.713262932	38.89213211	1950.01	5.7241716	38.891713	1749.47
5.713071448	38.89212904	1951.329	5.7241627	38.89167	1751.38
5.715333841	38.88883448	1979.973	5.7241438	38.891578	1757.68
5.714852839	38.88721826	1960.389	5.7241317	38.891519	1761.1
5.713829176	38.88848043	1961.071	5.7238258	38.89066	1787.3
5.713691429	38.89011013	1960.049	5.7239751	38.892016	1756.17
5.713004414	38.89213206	1961.248	5.7239118	38.891708	1756.31

5.712998195	38.8921488	1962.221	5.7238241	38.89191	1758.57
5.714456503	38.89077599	1980.61	5.7238188	38.891884	1765.33
5.715333841	38.88883448	1979.973	5.7236524	38.891704	1769.53
5.715526335	38.8855696	1920.013	5.7235411	38.891163	1774.19
5.715790133	38.88484558	1920.805	5.723595	38.892054	1761.74
5.71597718	38.88487022	1929.078	5.7235719	38.89257	1776.96
5.715854634	38.88538468	1919.244	5.7233833	38.892282	1782.74
5.71603711	38.88562628	1919.208	5.7233357	38.89205	1774.99
5.71560117	38.88613916	1920.245	5.7232995	38.891874	1782.19
5.715504506	38.88620686	1919.815	5.7232884	38.89182	1795.44

Table B.4 Cumulative displacement of InSAR measurement

Northing	Easting	Elevation	Cumulative displ
5.707085	38.890391	1898.2	-18.19
5.7071829	38.890868	1880.71	-31.54
5.7082484	38.896048	1823.2	42.03
5.7061528	38.885233	1920.11	42.4
5.706287	38.885884	1923.45	39.29
5.70686	38.888669	1917.28	20.72
5.7069698	38.889203	1893.19	25.49
5.7070649	38.889665	1905.47	-6.62
5.7070667	38.889674	1893.92	4.09
5.7071546	38.8901	1921.35	-51.87
5.7072211	38.890424	1907.19	-26.76
5.7072801	38.890711	1895.58	-26.04
5.7073129	38.890871	1889.85	-24.26
5.707338	38.890993	1886.55	-26.39
5.7073656	38.891127	1878.28	-28.96
5.7074193	38.891388	1873.38	-19.01
5.707641	38.892468	1820.02	39.66
5.707069	38.889056	1915.23	18.15
5.7072272	38.889825	1917.93	-25.73
5.7073581	38.89046	1932.15	-38.43
5.7074065	38.890697	1902.93	-27.42
5.7074654	38.890983	1881.91	-25.17
5.7075128	38.891214	1877.07	-23.59
5.707524	38.891268	1873.24	-24.26
5.7075739	38.891511	1872.77	-21.67
5.7064082	38.885216	1926.69	42.97
5.7065934	38.886116	1920.75	50.27
5.7071694	38.888915	1909.84	15.78
5.7072697	38.889403	1909.09	1.56
5.7075441	38.890737	1906.39	-32.65
5.7075625	38.890826	1902.96	-30.56
5.7070932	38.887916	1930.17	-39.34

5.7073024	38.888933	1917.3	15.71
5.7073874	38.889346	1915.31	-24.48
5.7074934	38.889861	1932.93	-44.82
5.7076299	38.890524	1915.64	-44.26
5.7076674	38.890707	1909.12	-27.13
5.7077234	38.89098	1896.03	-24.94
5.7077486	38.891102	1892.78	-21.41
5.7077604	38.89116	1879.88	-15.48
5.7077692	38.891203	1868.6	-17.82
5.7074401	38.888974	1914.61	11.41
5.7075775	38.889641	1925.78	-36.02
5.7078549	38.89099	1893.4	-18.39
5.7078739	38.891082	1890.24	-20.42
5.7079663	38.891532	1866.99	-12.69
5.7088246	38.895705	1826.33	49.68
5.7088298	38.89573	1822.65	48.65
5.7088843	38.895995	1824.42	48.59
5.7074859	38.888568	1913.62	20.69
5.7075179	38.888723	1913.74	20.4
5.7077186	38.889697	1940.29	-51.02
5.7079613	38.890878	1915.86	-25.31
5.70796	38.890872	1908.99	-30.29
5.7079899	38.891018	1895.61	-17.97
5.7080145	38.891137	1895.18	-26.36
5.7080166	38.891148	1886.9	-9.88
5.7087714	38.894818	1826.7	52.61
5.7087907	38.894911	1823.65	49.84
5.7080841	38.890846	1930.79	-33.17
5.7081609	38.89122	1884.31	-27.67
5.708168	38.891255	1881.54	-15.2
5.7082079	38.891449	1879.28	-10.32
5.7082202	38.891509	1879.07	-12.19
5.710426	38.902232	1748.12	182.38
5.7074798	38.887281	1919.96	23.84
5.7078184	38.888926	1926.82	-5.19
5.7079032	38.889338	1934.05	-54.06
5.7081715	38.890642	1928.39	-28.66
5.7081683	38.890627	1917.48	-22.76

Table B.5 Ground surface displacement results for validation

No	Ground survey measurement	InSAR measurement
1	5.254	0.21684
2	5.117	0.21097
3	5.1	0.20818
4	4.902	0.20321
5	4.671	0.20174
6	4.45	0.19749
7	4.426	0.1857
8	4.244	0.18559
9	3.868	0.17366
10	3.72	0.17007
11	3.711	0.1632
12	3.416	0.15808
13	3.356	0.15709
14	3.327	0.15214
15	3.274	0.14893
16	3.262	0.14714
17	3.016	0.14292
18	3.016	0.13943
19	2.83	0.13722
20	2.574	0.13705
21	2.452	0.13276
22	2.312	0.13094
23	2.232	0.12464
24	2.076	0.12452
25	1.879	0.12131
26	1.776	0.12039
27	1.584	0.11784
28	1.295	0.11274
29	1.055	0.10925
30	0.839	0.07097